Dynamic correction of geometric distortions in high-resolution functional MRI at ultra-high magnetic field strengths

Auteur : Di Bartolomeo, Katia
Promoteur(s) : Phillips, Christophe
Faculté : Faculté des Sciences appliquées
Diplôme : Master en ingénieur civil biomédical, à finalité spécialisée
Année académique : 2023-2024
URI/URL : http://hdl.handle.net/2268.2/20395

University of Liège - Faculty of Applied Sciences
University College London - Wellcome Center for Human NeuroImaging

DYNAMIC CORRECTION OF GEOMETRIC DISTORTIONS IN HIGH-RESOLUTION FUNCTIONAL MRI AT ULTRA-HIGH MAGNETIC FIELD STRENGTHS

GRADUATION STUDY CONDUCTED BY

KATIA DI BARTOLOMEO

WITH THE AIM OF OBTAINING THE MASTER'S DEGREE IN BIOMEDICAL ENGINEERING

Under the supervision of

Prof. Martina CALLAGHAN

Dr. Barbara DYMERSKA

Prof. Christophe PHILLIPS

ACADEMIC YEAR 2023-2024

Abstract

In neuroscience research, the use of functional magnetic resonance imaging (fMRI) at ultra-high ($\geq$7T) magnetic field strengths improves significantly the signal-to-noise ratio (SNR). However, fast imaging techniques like Echo-Planar Imaging (EPI) are prone to geometric distortions due to local field inhomogeneities, which become more pronounced at higher field strengths and can cause the mislocalization of relevant signal. To mitigate those distortions, conventional static correction methods use one "snapshot" fieldmap applied to all fMRI magnitude images. Other dynamic methods compute one fieldmap for each EPI time point from preliminary Gradient echo (GRE) images. By doing so, it accounts for the changes in the static magnetic field occurring during the acquisition time, including motion or breathing.

In this thesis, a new dynamic geometric distortion correction method is presented and compared to existing corrections. The technique uses a fieldmap computed from EPI images acquired with opposite phase encoding (PE) directions. This reference fieldmap is then used to estimate the constant phase offset present in all EPI phase data. A series of dynamic fieldmaps can thus be calculated from the EPI phase, and each volume is corrected independently. The main advantage of this method is to allow for a dynamic correction without the need for preliminary scans.

To perform a complete analysis of the methods, six different correction pipelines have been implemented. Two of them use a static fieldmap computed from GRE preliminary scans, with and without extra modelling of the susceptibility-by-motion effect. Two others compute a fieldmap from EPI volumes acquired with opposite PE direction, then apply it with and without the same extra model as before. Finally, two dynamic corrections have been implemented, estimating the phase offset based on preliminary GRE or on reversed PE acquisition. These methods have been tested on different datasets acquired at 7T at University College London, including one chin approach task inducing dynamic changes in the static field.

The results showed that for 3D EPI and small motion (<1mm translation and <1° rotation), using a static correction without extra modelling lead to a slightly better temporal stability. The dynamic corrections seem to induce extra variance, due to the extra computation steps present in the methods. However, to observe significant differences between the methods, the sequence and the task should be chosen wisely.

Future studies should focus on assessing the temporal behaviour of the different correction methods in a non-accelerated 2D unsegmented EPI sequence with greater head motion and a chin approach task. This would allow determining if this newly developed method visibly improves the temporal stability along the volumes.

Acknowledgments

This Master thesis was my first long-term project, giving me the opportunity to experiment the world of scientific research and the multiple challenges associated to it. During the development of this project, I always felt supported and helped by the right people. I certainly could not have completed this work without the contributions of multiple important individuals that I would like to sincerely thank.

First, I would like to express my gratefulness to Prof. Christophe Phillips, my supervisor and professor at the University of Liège, and to Prof. Martina Callaghan, the Head of Physics at the WCHN in London.They gave me the opportunity to work on such an interesting project and spend four incredible months in a challenging research centre in London.

Furthermore, I am sincerely grateful to my London supervisor Dr. Barbara Dymerska for her precious guidance and support throughout this project. From the very beginning, she was always available for answering any of my concerns and provided many wise revisions on the report. I must say that I never learned as much as working under her supervision. The realization of this project would never have been possible without her help.

I would also like to express my gratitude to the entire Physics team of the WCHN for the welcoming and friendly atmosphere. From the first day, they made me feel like I was part of the team. Moreover, they gave me enlightened advice regarding the presentation of my results.

Lastly, I cannot express enough my gratitude to my family for their infinite support throughout this project, and more generally throughout all stages of my studies. I feel incredibly lucky to be surrounded by such inspiring and motivating people. I am especially grateful to my parents for their trust, for always pushing me at my maximum and getting me back on track when I was lost. I am also grateful to them for allowing me to go abroad and live this unforgettable experience in London.

Contents

List of Figures

List of abbreviations

ABBREVIATIONS	FULL FORM
BOLD	Blood-oxygen-level dependent
CSF	Cerebrospinal fluid
DDC	Dynamic distortion correction
emf	electromotive force
EPI	Echo planar imaging
ETL	Echo train length
ESP	Echo spacing
FA	Flip angle
fMRI	functional Magnetic Resonance Imaging
GRE	Gradient echo
ICV	Intra-Cranial Volume
NMR	Nuclear magnetic resonance
PE	Phase encoding
PF	Partial Fourier
RF	Radio-frequency
SCOPE	Susceptibility Correction using Opposite Phase Encoding
SDC	Static distortion correction
SNR	Signal-to-noise ratio
TE	Echo time
TR	Repetition time
tSTD	temporal Standard Deviation
tSNR	temporal Signal-to-noise ratio
UHF	Ultra-high field
VSM	Voxel shift map

Introduction

High-resolution functional Magnetic Resonance Imaging (fMRI) has become a crucial tool in human neuroscience studies. The localization of functional brain networks can be achieved through this rapid and non-invasive imaging technique. Furthermore, ultra-high field (UHF) MRI systems ($\geq$7T) offer higher signal-to-noise ratio (SNR) and increased blood-oxygen-level-dependent (BOLD) contrast, thereby enabling higher spatial resolution imaging. However, this spatial precision is often compromised when employing very rapid functional imaging techniques such as Echo Planar Imaging (EPI). Indeed, in presence of inhomogeneities in the static magnetic field due to interfaces between tissues with different magnetic susceptibilities, EPI suffers from geometric distortions mainly in the phase-encoding (PE) direction.

Many methods have been developed to correct those geometric distortions and accurately re-localize neural activity. The first commonly used approach is based on computing a B_0 fieldmap from the phase change observed between gradient echo (GRE) images acquired at different echo times (TEs) (Jezzard and Balaban 1995). Another widely adopted approach, using only magnitude scans, estimates the fieldmap from two EPI images with opposing phase-encoding direction (Andersson et al. 2003). Once the fieldmap has been extracted using the former or the latter technique, the voxel shift/displacement map (VSM) can be computed and then used to unwarp all EPI volumes, resulting in undistorted images.

Nevertheless, a conventional static fieldmap fails to account for the dynamic changes of B_0 occurring during the scanning. To consider the potential variations of B_0, various dynamic approaches have been investigated. In the approach proposed by (Marques and Bowtell 2005.) (Lamberton et al. 2007), the EPI phase measured is decomposed into an offset (due to coil sensitivity) and a component proportional to the fieldmap and TE. Dynamic fieldmaps can then be derived at each time point by subtracting the phase offset from the phase measured throughout the EPI time series.

However, in such dynamic approach, estimating the phase offset from undistorted preliminary GRE scans may lead to inaccuracies. The time separation between GRE and EPI scans allows for significant changes in B_0 to occur, potentially reducing the accuracy of distortion correction. Moreover, adding GRE scans to the protocol is not always desirable, as the time the participant spends in the scanner can be quite long.

The motivation behind this project was to develop a combined approach for geometric

distortion correction. By using opposite PE direction scans, we are able to derive an initial fieldmap and thus extract the phase offset. Then, this phase offset is subtracted from the EPI phase volume-by-volume to obtain a series of dynamic fieldmaps. Therefore, each EPI time point is corrected, accounting for dynamic variations in field inhomogeneities. Moreover, there is no need for separate preliminary scans as the reversed phase-encoding EPI is directly embedded in the EPI run.

This thesis is divided into five chapters. The first chapter aims to describe the general background by reviewing theoretical notions considered during the work. Chapter two describes the data collection and the different distortion correction approaches implemented, including static field mapping from GRE, static field mapping from opposite PE scans, dynamic fieldmaps with phase offset estimation from GRE data and the combined dynamic method with phase offset estimation based on opposite PE scans. In this chapter, qualitative and quantitative methods to assess the robustness of each approach are also presented. The results obtained are then shown in the third chapter. The fourth chapter contains a critical analysis of those results. Finally, the last chapter concludes by discussing the limitations of this study and the potential future improvements.

All MATLAB code developed in this project can be found in a GitHub repository, to which you can have access upon request.

Chapter 1

Background

1.1 Magnetic resonance imaging

Magnetic resonance imaging (MRI) is currently one of the most widely used medical imaging techniques. Its high image quality and non-invasiveness make it very attractive for diagnostic and research purposes, especially in the neuroscience area. Since its creation in the 1970s[5], the increasing interest of scientists to understand anatomical and physiological behaviour of the human body has led to continuous development of MRI techniques and its applications.

Due to the absence of ionizing radiation, MRI is particularly valuable in neuroscience research and in the monitoring of a broad range of pathologies. Moreover, with its great flexibility and ability to characterize a large variety of tissue properties, MRI has become one of the most significant breakthroughs of the century.

1.1.1 Physical principle

MRI is based on the interaction between an applied magnetic field and a nucleus with a nuclear magnetic moment. Multiple nuclei have a non-zero spin, providing them with a nuclear magnetic moment. The most abundant nuclei in living organisms are hydrogen protons, due to their substantial presence in water and fat [6]. For this reason, hydrogen protons are the nuclei of interest for medical MR imaging.

Initially, the spins are oriented randomly. Nevertheless, when placed under a strong external magnetic field B_0, a large number of protons become polarized and align with the direction of B_0, precessing around it. The precessing frequency, also known as the Larmor frequency, is proportional to the strength of the external magnetic field [7]:

$$\omega_0 = \gamma B_0 \tag{1.1}$$

with γ representing the gyromagnetic ratio, a constant value for each nucleus ($\gamma_{protons} = 42.58 MHz/T$).

There are two different energy levels for hydrogen atoms described as "up" and "down". A slightly smaller number of nuclei are oriented antiparallel to the B_0 field ("down"). The number of spin parallel to B_0 exceeding the number antiparallel to that field is known as the "spin excess" and is very small [8]:

$$\text{spin excess} = N\frac{\hbar\omega_0}{2kT^\circ} \tag{1.2}$$

with N, the total number of protons in the sample, $\hbar$ the Plank constant, k the Boltzmann constant and T° the temperature.

This excess yields to a net longitudinal magnetization M_z parallel to B_0. For a sample with ρ_0, the number of protons per unit volume (or spin density), the net longitudinal magnetization M_z is given by the proton magnetic moment $\gamma\hbar/2$ multiplied by the spin excess per unit volume. Taking into account Equation 1.1, it gives [8]:

$$M_z = \frac{\rho_0\gamma^2\hbar^2}{4kT^\circ}B_0 \tag{1.3}$$

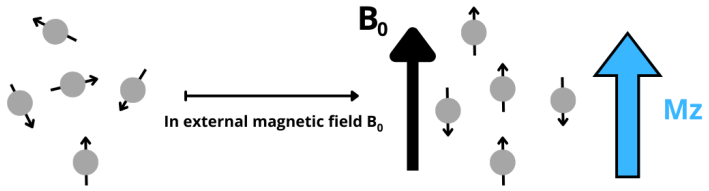

Figure 1.1: Longitudinal magnetization M_z.

At this stage, no net transverse magnetization M_{xy} exists because even though the spins are precessing at the same frequency ω_0, their phases are random.

When a varying magnetic field B_1 is applied using a radio-frequency (RF) pulse at the Larmor frequency ($\omega_{RF} = \omega_0$), the resonance phenomenon occurs. The energy provided flips the magnetization vector Mz from the z-axis towards the xy-plane (Figure 1.2). If the RF pulse causes the magnetization to flip by a 90° angle, the net magnetization will then precess in the transverse plane with frequency ω_0. No net longitudinal magnetization is now detected, but the spins precess at the same frequency and with the same phase in the xy-plane, leading to a net transverse magnetization. With other flip angles, the longitudinal magnetization M_z decreases to non-zero values as M_{xy} increases.

1.1.2 Relaxation times

When the excitation of the RF pulse stops, the spins go back to their equilibrium state by two independent relaxation processes: longitudinal relaxation and transverse relaxation, characterized by time constants T_1 and T_2 [5].

T_1 is the time during which there is a regrowth of 63% of the longitudinal magnetization M_z initial value [9]. Similarly, T_2 is the time constant that determines the

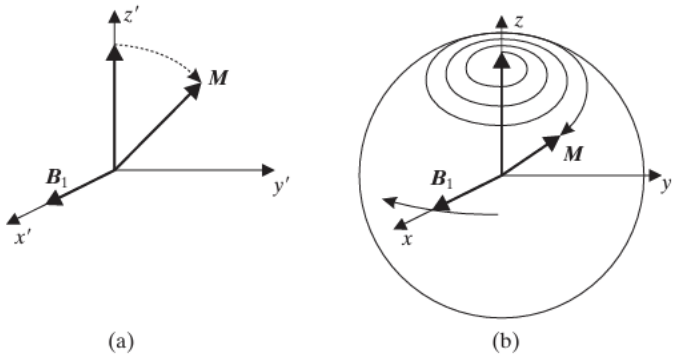

Figure 1.2: Magnetization vector motion in rotating (a) and static (b) frame (adapted from [5]).

rate at which excited protons go out of phase with each other, inducing a decay of the transverse component M_{xy} of the field as seen in Figure 1.3. T_2 is defined as the time after which the transverse magnetization has decreased to 37% of its initial value. Those time constants define the evolution Equation 1.4 of the magnetization:

$$\begin{cases} M_z = M_0(1 - e^{-t/T_1}) \\ M_{xy} = M_0 e^{-t/T_2} \end{cases} \tag{1.4}$$

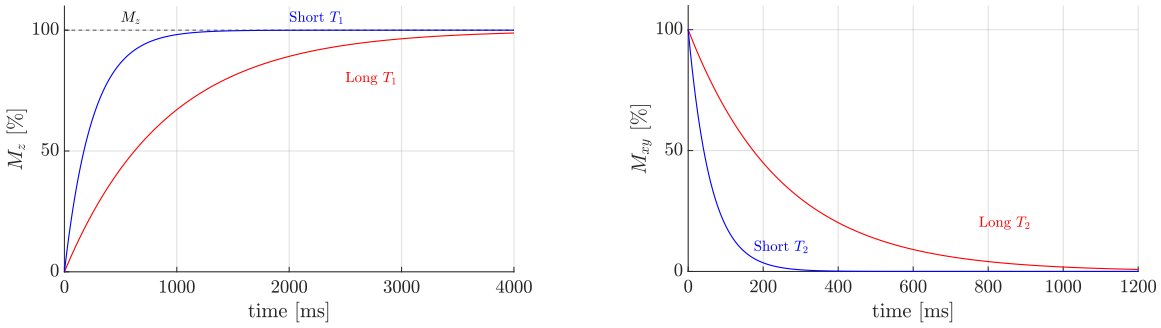

Figure 1.3: Relaxation processes (reproduced from [9])

.

However, in real conditions, the transverse magnetization M_{xy} decays much faster due to the inhomogeneities present in the main magnetic field. This faster decreasing rate is called T_2^* and is given by [5]:

$$\frac{1}{T_2^*} = \frac{1}{T_2} + \frac{1}{T_2'}$$

Considering that T_2' is the time constant linked to the contribution of the total relaxation attributable to the magnetic field inhomogeneities.

1.1.3 Hardware

MRI systems come in various sizes, yet they always consist of four major components: a main magnet, gradient coils, RF coils, and computer systems including the visualization console [7]. As illustrated in Figure 1.4, the coils are arranged in a concentric way within the cylindrical magnet.

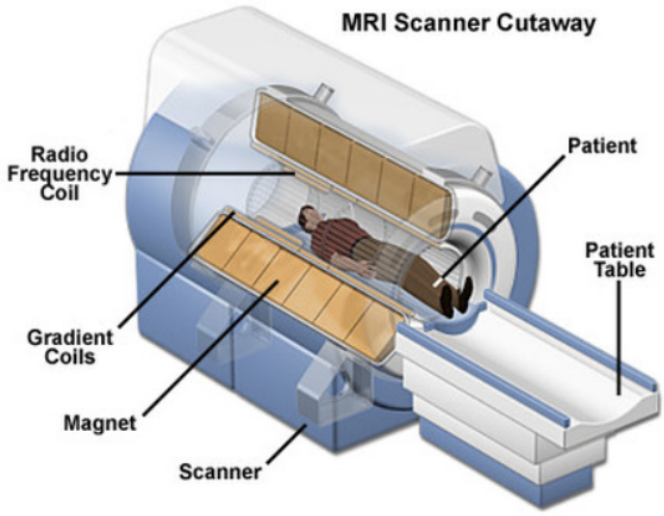

Figure 1.4: MRI scanner components (adapted from [10])

.

Main magnet

The main magnet is the heart of the MRI scanner as it produces the strong static magnetic field B_0. The most common type of magnet used is a superconductive magnet which consists of a series of coils wound on a cylindrical form within a bath of liquid helium enclosed in a cryostat [11].

Gradients

Usually, gradient coils (also called gradients) are a combination of three orthogonal sets of coils, one for each of the physical x, y, and z directions. Their principal function is to allow for spatial encoding of the MR signal. This is achieved by providing a temporary change in the magnitude B_0 as a function of position [5].

Specifically, when activating all three coils simultaneously with strengths Gx, Gy, and Gz, respectively, the main field ideally varies in space as [5]:

$$\mathbf{B}(x, y, z) = (B_0 + G_x x + G_y y + G_z z)\hat{\mathbf{z}}$$

In this expression, G_x, G_y and G_z are the constant gradient amplitude which have units of Gauss per centimetre. In MR imaging methods, the gradients are switched on and off very rapidly.

RF coils

RF coils have two purposes: they are used to send RF pulses and to receive the signal back from the patient's body. RF coils can function as a transmitter, a receiver or both [5]. When acting as a transmitter, they generate a time-varying B1 magnetic field which is perpendicular to the main B_0 field. The energy transmitted by RF pulses flips magnetization away from the z-axis. When this deviation reaches any angle α, it's referred to as a α° pulse. Receiver RF coils catch the oscillating net transverse magnetic flux M_{xy} produced by excited spins, inducing a voltage according to Faraday's Law of induction.

Computer system

There are multiple computer systems embedded into an MRI machine to control all the scanner functions [5]. They work interdependently to control the RF and gradient pulses, to sample the incoming signal and to process the data to produce and display the generated images.

1.1.4 MRI signal

The signal picked up by the receiving coils is an induced voltage generated by the precession of the net transverse magnetization [7]. This signal is always a complex number that can be represented on the real-imaginary plane. The signal can thereby be reconstructed in multiple ways [9]:

- "real" image,
- "imaginary" image,
- Magnitude (M) image,
- Phase (φ) image.

Usually in clinics, magnitude images are the only one used for diagnostic. However, sometimes, phase data is also saved for some specific applications. The phase of the signal is given by the following formula:

$$\varphi(x,y,z) = 2\pi \mathrm{TE} \cdot \underbrace{\Delta\omega_0(x,y,z)}_{\text{Fieldmap}} + \underbrace{\varphi_0(x,y,z)}_{\text{Phase offset}} \tag{1.5}$$

It consists of two components: one is proportional to the fieldmap and the echo time (TE) and the other is the phase offset, representing mainly the phase of coil sensitivity profile [3][4]. This phase offset has been proved to stay relatively constant over time and subject motion [12].

1.1.5 Image formation

To form an image, the goal is to find the signal intensity of each pixel. However, in MRI scanners, the signal is picked up by the coils without knowing where it comes from.

To be able to visualize a proper image, the MRI system encodes the spatial position of the signal [7].

In multi-slice 2D images, a first gradient is applied during the RF pulse in the Z direction to select the slice. Since the Larmor frequency is proportional to the applied field, the slice is selected by emitting an RF pulse at the Larmor frequency of the desired slice.

Then, during relaxation, 2 different gradients are applied to localize the signal within the 2D slice. One of the gradients, usually applied in the X-direction, encodes the position by modifying the precessional frequency along the X-axis. This process is called frequency encoding. Then, by applying a gradient in the Y-direction, the spins along the Y-axis get dephased, and it allows to encode for the position across this axis. This Y-gradient is also known as the phase encoding gradient. Each Frequency and Phase Combination defines its location within a slice.

All the data collected is organized into an array called the K-space, where each point contains spatial frequency and phase information about every pixel in the final image [9]. Then, with a reconstruction algorithm, which most of the time is the Fourier transform, the k-space information is converted into an image as we can see in Figure 1.5. Changing the way the K-space is sampled modify the final MR image.

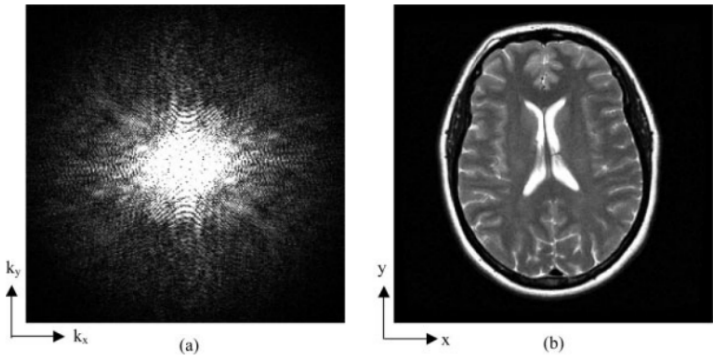

Figure 1.5: Raw data in K-space and corresponding image data in image space (adapted from [13])

.

1.2 Functional MRI

As mentioned in its name, fMRI is based on MRI physical and image formation principles. This imaging method has been developed to observe time-varying changes in brain activity [14]. fMRI is one of the most widely used imaging techniques in cognitive neuroscience studies but also in presurgical planning [15].

1.2.1 BOLD signal

As stated before, in fMRI, the goal is to observe brain activity. BOLD contrast mechanism is usually used to visualize neural activation. When the activity of a local region of the brain increases, cerebral blood flow increases, delivering more oxygenated hemoglobin in the capillaries [14]. BOLD contrast arises from the change in magnetic field surrounding the red blood cells depending on the oxygen state of the hemoglobin. When hemoglobin is fully deoxygenated (Hb), it is paramagnetic whereas, when fully oxygenated (HbO_2), it's diamagnetic. Therefore, Hb will cause local dephasing of protons, reducing the returned signal from the tissues nearby. T_2^* weighted sequences are used to measure this change, which is in the order of 1-5%.

1.2.2 Sequences

The goal of fMRI being to observe time-varying behaviour, having a good temporal resolution is particularly important. In order to reduce the acquisition time, different imaging techniques have been developed.

GRE

A first way to increase the speed of the sequence is to use gradient echo instead of spin echo in which two RF excitations are needed. In GRE, the frequency encoding gradient is used twice to create the echo (Figure 1.6). First it is used to produce transverse dephasing of spinning protons and then right after, it is reversed and used as a readout gradient to realign the dephased protons and thereby acquire the signal. Compared to spin echo sequences, GRE are much faster since they only have one RF pulse per TR, they can have relatively short TR and create fast images.

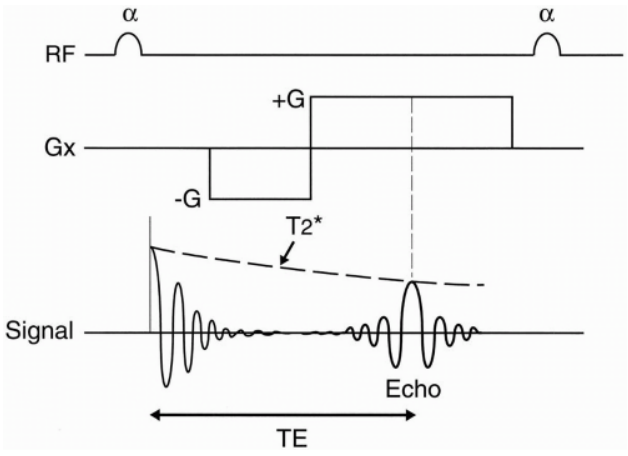

Figure 1.6: GRE pulse sequence with gradient reversal to create an echo (adapted from [16])

Echo train

In gradient echo train sequences, a series of echoes is generated by a sequence of gradients following the RF excitation. The readout or frequency encoding gradients are quickly and repeatedly reversed to collect multiple lines of K-space data after only one RF pulse. It enables us to collect data much faster.

2D EPI

Echo planar imaging is a specific gradient echo train sequence where the complete K-space is acquired following only one excitation RF pulse. As we can see in Figure 1.7, the readout gradients (G_x) are reversed rapidly to acquire the complete K-space during a single T_2^* decay. Each positive or negative lobe of this gradient correspond to a different k_y line in K-space. Currently, the most used EPI technique is the so-called blipped-EPI as the phase-encoding gradient (G_y) is applied briefly during the time when the readout gradient was zero. The obtained K-space trajectory is simply sweeping straight lines from left to right, and then from right to left.

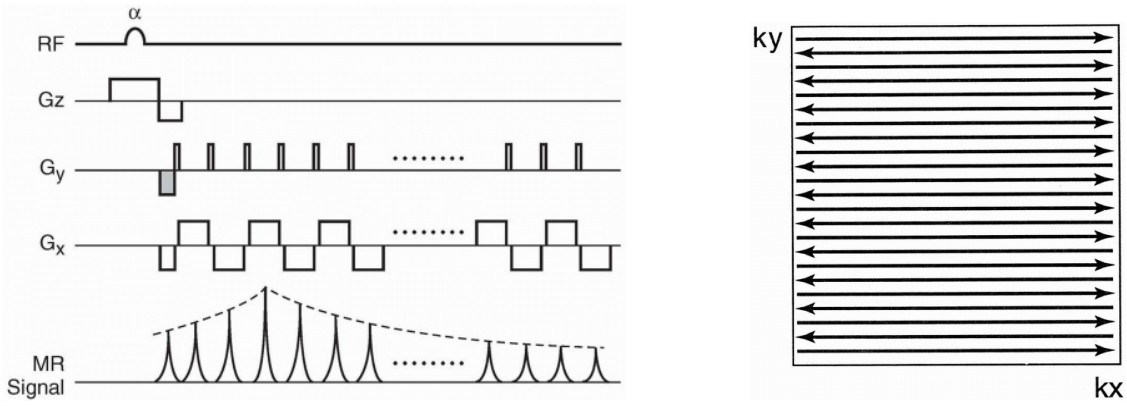

Figure 1.7: blipped-EPI pulse sequence (left) and the corresponding K-space trajectory (right) (adapted from [16])

This fMRI technique is very fast and has low power deposition because only one RF is needed by slice. Nevertheless, it presents an important disadvantage. It is very prone to off-resonance artefacts because the phase accumulates along the entire readout. Distortion in EPI is most pronounced in the PE (y-axis) direction because of the long time between sampling points (low bandwidth) relative to the readout direction (high bandwidth). During this time, there can be a substantial change in phase accumulation due to field inhomogeneities presented in 1.3.

Depending on the way K-space is traversed (bottom-up or top-down), the voxels are stretched or compressed. Blip up and blip down acquisition therefore lead to the same amount of distortion but in the opposite direction (Figure 1.8).

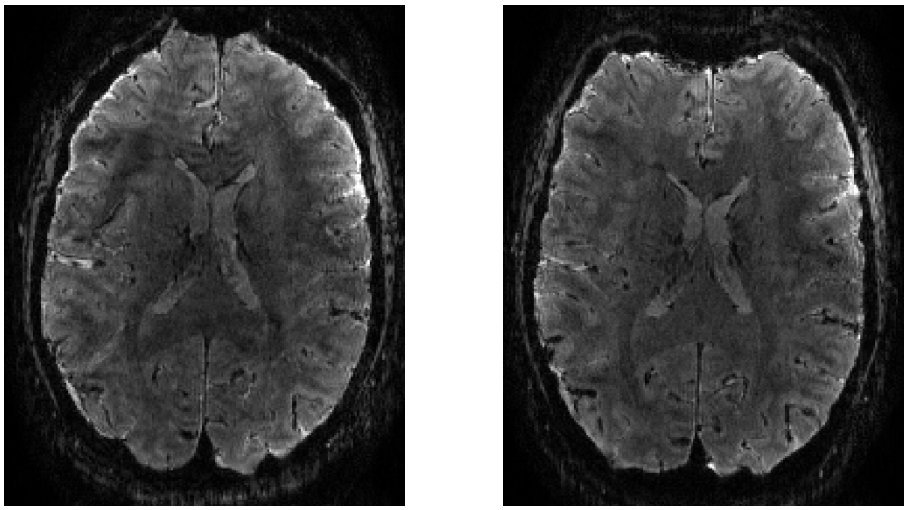

Figure 1.8: EPI images acquired traversing K-space bottom-up (left) and top-down (right)

1.3 B_0 field inhomogeneities

As stated in the previous section, EPI suffers from geometric distortions in the PE direction in the presence of B_0 field inhomogeneities. These geometric distortions arise from the spatial variation of B_0 causing differences in Larmor frequency and signal mislocalization. The cause of those B_0-inhomogeneities can have different origins. They can be directly due to the hardware or specific to the tissue scanned. The two main sources of tissue-related B_0 geometric distortions are chemical shifts and susceptibility differences.

1.3.1 Chemical shift

Chemical shift consists of small changes in the resonant frequency due to different environments of nuclei. For example [9], the ^{1}H protons of fat, which can be found within a long triglyceride chain, are enveloped by clouds of electrons. These clouds act as partial shields, mitigating the impact of an externally applied magnetic field on the fat protons. In contrast, the ^{1}H protons of water are less shielded as the highly electronegative oxygen atom pulls their electron clouds away from them [17].

Due to those different shielding, a fat proton experiences a slightly weaker local magnetic field. Their resonance frequency is thereby a little lower than a nearby water proton. This small difference in frequency is approximately 3.5ppm (or 3.5×10^{-6}). It must be noted that chemical shift between two species produces both a frequency and a phase shift between them. This suggests that both frequency and phase encoding processes are impacted.

In MR image reconstruction, spatial position along the frequency-encoding direction is assigned based on the resonance frequency. If, within one voxel, both water and lipid protons coexist, the signal emitted by the lipid protons will have a lower frequency than the one from the water protons.

Therefore, if the reference frequency of the system is set to water, the signal coming from the fat protons appears to originate from water protons from another voxel in a lower part of the field [18].

As stated in 1.2.2, in EPI, the bandwidth per pixel in the frequency-encoding direction is very large, making chemical shifts in this direction unnoticeable. However, in the phase-encoding direction, the bandwidth per pixel is extremely small. At 7T, the Larmor frequency is approximately 300MHz and the fat/water chemical shift is [9]:

$$\Delta f = 300\text{MHz} \times 3.5\text{ppm} = (300 \times 10^6)(3.5 \times 10^{-6}) = 1050\text{Hz}$$

In EPI sequences, chemical shifts lead to B_0-field inhomogeneities and with a very low phase-encoding bandwidth, artefacts in this direction become visible.

1.3.2 Susceptibility differences

Magnetic susceptibility (χ) is a measure of how a material becomes magnetized when it's placed in an external magnetic field. Some materials strengthen the field ($\chi > 0$) by concentrating it [9] . These are called paramagnetic, superparamagnetic, or ferromagnetic, depending on the extent of the effect. Other materials, called diamagnetic materials, weaken the magnetic field by dispersing it. If an object has non-homogeneous susceptibility, it leads to a non-uniform magnetic field [17].

In Table 1.1, we can see that molecular oxygen, O_2, is weakly paramagnetic, which means that its internal magnetization is slightly higher than B_0. On the other hand, most biological tissues are diamagnetic and oppose the B_0 magnetic field. Therefore, distortions can be observed at natural interfaces between air and tissue. Moreover, ferromagnetic materials have the largest susceptibility inducing prominent field distortion and artefacts around metal implants.

Magnetic property	**Magnetic susceptibility, χ (in ppm)**	**Example material**
Diamagnetism	-10	Water, most biological tissues
Paramagnetism	+1	molecular oxygen, O_2
Superparamagnetism	+5000	SPIO contrast agents
Ferromagnetism	>10 000	Iron, steel

Table 1.1: Magnetic susceptibilities of different materials (adapted from [17]).

The amounts of off-resonance local field depend directly on the B_0-field strength. At ultra-high field (UHF), magnetic susceptibility difference at air-tissue boundaries is the largest source of B_0-field inhomogeneities [17].

In brain imaging, two main air-tissue boundaries cause distortions of the image inside the brain. The first most visible artefacted region is located near the sinuses and consists mainly of the frontal pole and the orbitofrontal cortex. Another significantly affected region is the medial temporal lobe, which is close to the ear canals.

1.4 Ultra-high field MRI

Ultra-high magnetic field strength MRI systems are scanners with a main magnet that provide a B_0 static magnetic field of at least 7T. Their main advantage is their increased sensitivity. Indeed, electromotive force induced by the receiving coils is given by [8]:

$$emf = -\frac{d}{dt}\int d^3r \vec{M}(\vec{r},t)\cdot\vec{\mathcal{B}}^{\text{receive}}(\vec{r})$$

where $\vec{\mathcal{B}}^{receive}$ is the receive field, also known as B_1. Neglecting any spatial variations and considering that the magnetization can be written $M(t) = M_z e^{-i\omega_0 t + i\phi_0}$, the emf is proportional to $\omega_0 M_z$. From equation 1.3, the signal caught by the receiving coils then depends quadratically on the static magnetic field B_0 [8]:

$$\text{signal} \propto B_0^2$$

This results in an increased SNR as the noise only has a linear B_0 dependency at UHF [19]. The improved SNR can be used to increase spatial resolution and better differentiate between small anatomical structures. Moreover, in fMRI the time series SNR also get enhanced leading to a greater sensitivity to temporal correlations in the BOLD signal.

On the other hand, as depicted in Section 1.3.2, the extent of off-resonance local field is proportional to the static magnetic field. Therefore, at UHF, more susceptibility-induced artefacts can be observed. In neurosciences, as some structures of interest are of particularly small sizes, UHF MRI can be used to obtain better spatial resolution. The increased distortions then need to be accounted for and reduced as much as possible.

1.5 Existing approaches

These geometric distortions have been proved to be extremely problematic in clinical assessment and pre-surgical planning [15]. A shift in neural activation could indeed induce the misidentification of essential functional regions and impact the surgical approach.

1.5.1 Acquisition stage

Multiple methods have been developed in the acquisition stage to mitigate those artefacts. In this section, some existing methods are presented.

Water excitation

The B_0 inhomogeneities due to chemical shift presented in 1.3.1 can be avoided. Since the frequency offset between water and fat stays the same everywhere and fat signal is not of interest in fMRI, it can be suppressed or not excited.

In the data used in this thesis, water-selective excitation was used to get rid of these artefacts. By using a binomial RF pulse, water is selectively excited and fat protons' resonance frequency is unchanged.

Thanks to this process, only one main source of geometric distortions due to B_0 inhomogeneities is left to deal with.

Shimming

The B_0 magnetic field is supposed to be static and unchanging over time. However, as stated in Section 1.3, tissue properties can create inhomogeneities leading to geometric distortions. Moreover, even following the most rigorous manufacturing tolerances, the magnet's field is not perfectly uniform after production.

Shimming is the process used to maximize B_0 field homogeneity. First, the real magnetic field is accurately measured [20], then entered into a computer program to calculate the correction needed. On most scanners, two shimming techniques are usually implemented: passive and active shimming.

Passive shimming consists of designing and placing small pieces of ferromagnetic material at specific locations within the magnet bore. Through their passive response to B_0, this process tailors the magnetic field distribution towards a more uniform state [21]. Passive shimming is not the most straight-forward procedure, as it requires adding pieces of material in the unit. Therefore, it is not used for patient-specific shimming but rather for the static removal of hardware-related and environmental sources of field imperfection. The main drawback of this method is that the shim material is sensitive to temperature changes. In EPI sequences, as the gradient must be switched on and off very rapidly, the bore tends to heat, causing a change in the magnetic distribution created by the shim.

When a patient is placed in the scanner, specific tissue-related B_0 inhomogeneities arise. Active shimming is a method to correct those individual non-uniformities from patient to patient. Field inhomogeneities are measured and visualized on a B_0 map [20]. Currents are then directed into shimming coils, generating induced corrective magnetic fields. Their purpose is to cancel the remaining field gradient within the bore. Before scanning begins, automated shimming is usually performed on many MRI scanners to obtain the most uniform field as possible.

Accelerated acquisitions

In order to reduce the geometric distortions due to phase accumulation along the phase encoding direction, a solution is to reduce the time between the acquisition of two lines in K-space. This time is called the echo spacing (ESP).

In accelerated acquisitions, some K-space lines are skipped, reducing the time between adjacent lines. By using a proper image reconstruction algorithm, the missing lines are reconstructed using the redundant information from RF receive coils. To account for that, another metric is defined: the effective ESP. This represents the real ESP between two adjacent lines, accounting for the acceleration factor:

$$\mathrm{ESP}_{\mathrm{eff}} = \frac{\mathrm{ESP}}{\text{accelerating factor}}$$

By accelerating the acquisition, the phase has less time to evolve in the phase-encoding direction, resulting in reduced B_0 inhomogeneities and geometric distortions.

Multi-shot EPI

Another way of reducing the ESP_{eff} is to use multi-shot EPI. In single-shot EPI, since all lines of K-space are acquired after only one RF stimulation, the phase errors due to magnetic susceptibility artefacts tend to accumulate along the entire phase-encoding gradient. Multi-shot, or segmented, EPI is a technique to reduce this phase accumulation and therefore the geometric distortions associated. Multiple RF excitations are required [8], and the same method as in single-shot EPI is used to cover smaller regions of K-space after each RF pulse (Figure 1.9). Thereby, the entire K-space is divided into N_s segments and acquired after N_s RF pulse [16] . The resulting K-space data is then combined to form the complete K-space. The total number of lines in the k_y direction is given by: $N_y = N_s \times \text{ETL}$, with ETL, the echo train length, which is the number of lines/echoes in each segment.

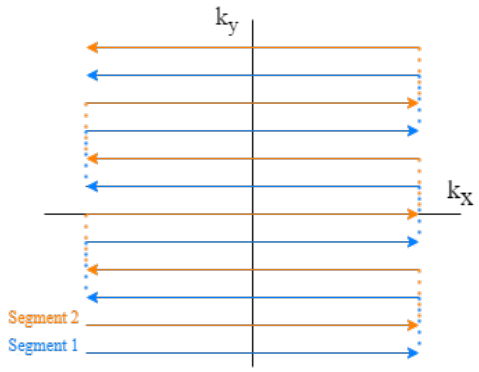

Figure 1.9: K-space trajectory of multi-shot interleaved EPI with 2 segments

As in accelerated acquisitions 1.5.1, the ESP is reduced in multi-shot EPI. the effective ESP is given by:

$$\text{ESP}_{\text{eff}} = \frac{\text{ESP}}{\text{nb segments}}$$

With the K-space trajectory presented in Figure 1.9, the ESP is decreased by a factor 2, giving twice less time for the phase error to accumulate and leading to fewer geometric distortions.

However, the main drawback emerging from this technique is that it takes longer to perform compared to single-shot EPI causing it to be more susceptible to motion artefacts.

1.5.2 Post-processing

To mitigate the residual field inhomogeneities and resulting geometric distortions, techniques have also been developed in the post-processing stage. Usually the process involves using a static B_0 fieldmap or a series of fieldmaps for each time point. This

fieldmap can be converted to Voxel Shift Map (VSM) showing how much each voxel has to be shifted in the phase-encoding direction to create a distortion-free image.

Static corrections

Static correction strategies use only one VSM to unwarp the entire EPI time series. Distortions can be corrected using a B_0 fieldmap derived from the phase difference between GRE images acquired at multiple TE's [1]. This method requires the phase data of preliminary GRE scans.

Another technique based only on magnitude data and that doesn't involve pre-scans is also commonly used to correct for geometric distortions [2]. Two echo-planar images are acquired with opposite PE direction: one traversing K-space bottom-up and the other one top-down. The resulting images have distortions with equal magnitude but opposing directions. The algorithm then estimates the voxel displacement map by trying to minimize the difference between the two scans.

Dynamic corrections

However, the use of a single fieldmap doesn't account for dynamic changes in B_0 during the fMRI run due to motion, breathing or heating of the gradient coils. Multiple dynamic correction methods have therefore been developed.

The technique implemented in SPM [22] *"Realign & Unwarp"* module [23], models geometric distortion only from EPI magnitude scans. The static fieldmap is modified at each time point, taking into account the motion parameters estimated to consider the susceptibility-distortion-by-movement interactions. It provides a good approximation of the B_0 field changes due to motion, regardless of the other causes such as breathing or gradient heating.

To obtain a more complete correction, a fieldmap can be generated for each time point using the phase EPI data. The phase measured contains an offset and a component proportional to the fieldmap and TE. The dynamic series of fieldmaps can thereby be obtained by subtracting the phase offset from the phase data at each time point [3][4]. Those methods are based on the assumption that the phase offset remains stable over time and during motion. A previous study at 7T [12] has confirmed this assumption showing that with large shifts in head position, the changes in the phase offset are around two order of magnitude lower than the B_0 field variations. Nevertheless, preliminary GRE scans are used to compute the first fieldmap from which the phase offset is estimated, which may cause potential correction errors.

1.6 Aim of the thesis

As the use of fMRI at UHF increases in neuroscience research, the need for undistorted scans with correctly located activity becomes crucial. The goal of this thesis was to develop a dynamic distortion correction [3][4] taking into account the changes in B_0

due to motion and breathing during the scanning. To avoid the need for preliminary GRE scans, the initial fieldmap from which the phase offset is derived, is computed with magnitude blip-opposed EPI scans as in the static correction in [2]. By doing so, the reference scans would directly be embedded in the EPI run, obviating the need for additional GRE images. In this thesis, I implemented the combined approach and compared it with existing techniques with quantitative assessment tools.

Chapter 2

Methods

In this section, the data collection and the different pipelines implemented to correct for the geometric distortions will be explained. Next, the assessment method for evaluating the temporal stability and distortion correction accuracy of the implemented correction pipelines will be detailed.

2.1 Distortion correction methods

During this research project, six main pipelines have been developed to correct for geometric distortions (Figure 2.1). These pipelines either replicate already existing distortion correction methods or seek improvement in the correction accuracy by appropriate modifications, as explained below. Each of these methods delivers one or multiple fieldmaps $\Delta\omega_0$. Static distortion correction (SDC) uses a unique fieldmap capturing the main field inhomogeneities, whereas dynamic distortion correction (DDC) uses a series of fieldmaps to account for the additional dynamic effects. The fieldmap can be converted into Voxel Shift Maps (VSMs) showing how much each voxel needs to be shifted in the phase-encoding direction in order to bring it to a distortion-free space:

$$\mathrm{VSM} = \Delta\omega_0 \cdot \mathrm{M_{PE}} \cdot \mathrm{ESP_{eff}}\ [\text{voxels}] \tag{2.1}$$

with $\Delta\omega_0$ the fieldmap, M_{PE} the matrix size in the PE direction and ESP_{eff} the effective echo spacing. These VSMs are used to unwarp the distorted data and obtain distortion-free images.

2.1.1 Static field mapping with GRE (Gradient echo)

Theory

The first method, described by (Jezzard and Balaban 1995) derives a static fieldmap from multiple GRE phase images. By acquiring GRE scans at multiple TEs, the fieldmap can be extracted by estimating the slope $\Delta\omega_0$ of the linear regression $\varphi = 2\pi\mathrm{TE} \cdot \Delta\omega_0 + \varphi_0$

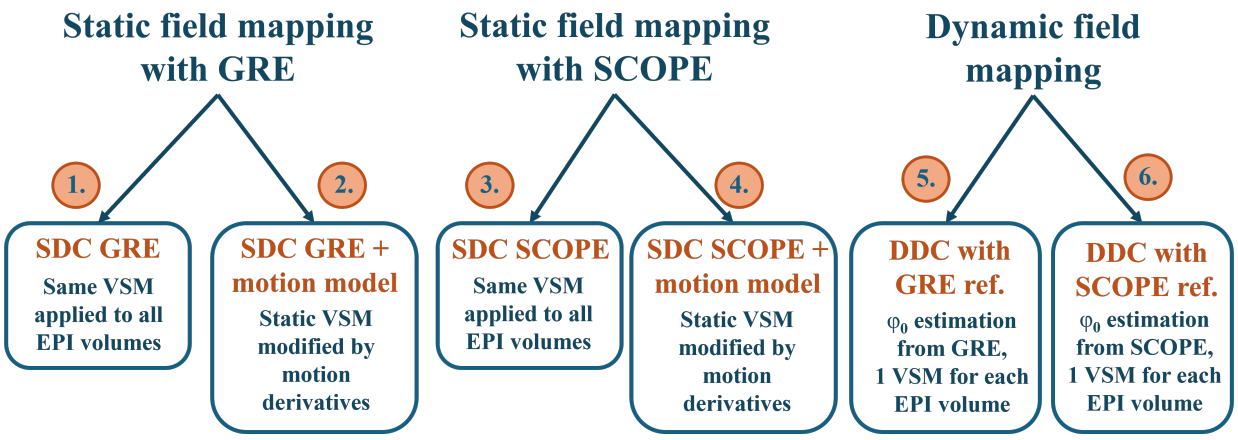

Figure 2.1: Summary of the six correction pipelines developed. They can be split into 3 groups: two of these, using static field mapping with Gradient echo (GRE) and SCOPE, with or without modification of the VSM with head movements. The last one employs a fully dynamic field mapping with one VSM per volume derived with GRE or SCOPE reference used to estimate the phase offset φ_0.

where φ and TE are the independent variables. If we consider the case using only two TEs, the phase signals described in Equation 2.1.3 are given respectively by:

$$\varphi_{\mathrm{TE}_1}(x,y,z) = 2\pi \mathrm{TE}_1 \cdot \Delta\omega_0(x,y,z) + \varphi_0(x,y,z)$$
$$\varphi_{\mathrm{TE}_2}(x,y,z) = 2\pi \mathrm{TE}_2 \cdot \Delta\omega_0(x,y,z) + \varphi_0(x,y,z)$$

The fieldmap can thereby be easily extracted by subtracting the phase of the two GRE images [1]:

$$\Delta\omega_0 = \frac{\varphi_{\mathrm{TE}_2} - \varphi_{\mathrm{TE}_1}}{2\pi(\mathrm{TE}_2 - \mathrm{TE}_1)} = \frac{\Delta\varphi}{2\pi\Delta\mathrm{TE}} \tag{2.2}$$

This unique fieldmap is then applied to all EPI volumes.

Implementation

The complete diagrams of the pipelines are presented in Figure 2.2. The phase of the GRE scan at all TEs is first unwrapped with the ROMEO unwrapping tool [24] and the $\Delta\omega_0$ fieldmap is calculated as a weighted echo averaging assuming linear phase evolution with time. SPM12 [22] segmentation tool is used to create a probability map of being inside the brain. Then this map is binarized to generate an intra-cranial volume (ICV) mask. The fieldmap is masked and then smoothed and extrapolated outside the brain boundaries with *"smoothn.m"* which is a fast and robust discretized spline smoother for data of arbitrary dimension. This open-source function by D. Garcia can be found in MathWorks "File Exchange" [25]. The VSM is computed using Equation 2.1 before being co-registered using SPM12 [22] to the EPI volume closest in time.

To unwarp the functional data using this VSM and correct for the geometric distortions, two different methods have been implemented.

SDC GRE

The first method is purely static and consists of combining volume-by-volume motion and distortion correction in a single interpolation step. To do that, the motion with respect to the reference EPI volume was estimated using SPM12 [22] *Realign (Estimate)*. This step modifies the 4x4 *mat* header of the NIfTI files to account for the transformation matrix, bringing the target volume to the space of the reference volume.

The absolute motion of each volume i is then computed by solving the following equation:

$$M_{\text{abs,i}} = \text{mat}_i \cdot \text{mat0}_{\text{ref}}^{-1}$$

with mat_i, the matrix containing the relative motion between volume i and the reference volume,
mat0_{ref}, the matrix containing the position of the reference volume with respect to the scanner.

A warp field containing each voxel coordinates (x,y,z) is created, and the static VSM accounting for the geometric distortion is added in the PE (y) direction. This step modifies the coordinate of distorted voxels in the PE direction. The motion matrix is then multiplied to this corrected field to correct for motion with respect to the reference volume. Finally, with a single step interpolation, both motion and distortion correction are applied at once for each volume. In this method, the VSM used is static, which means the same VSM is used for all the volumes within the EPI time series.

SDC GRE + motion model

The second pipeline uses the same VSM computation but unwarps EPI data using SPM12 [22] *"Realign & Unwarp"*. In this module, the motion and distortion correction are also applied in a single step (i.e. involving only one interpolation step). Additionally, dynamic field changes due to motion are modeled using affine transform matrices describing motion with respect to reference volume and a static fieldmap acquired before the EPI time series. Partial derivatives of the deformation field are estimated based on the affine transformation for each EPI volume and added on top of the static warp field. This is done in an iterative process to account for the susceptibility-by-motion interactions [23] [26].

Other sources of dynamic field changes such as breathing, eye movements or swallowing, which can be well decoupled from head motion, are not modeled by this method.

2.1.2 Static field mapping with SCOPE

Theory

In this pipeline, two EPI scans with reverse PE direction were used to estimate the fieldmap. By acquiring one image blip-up and the other one blip-down, both are subject to

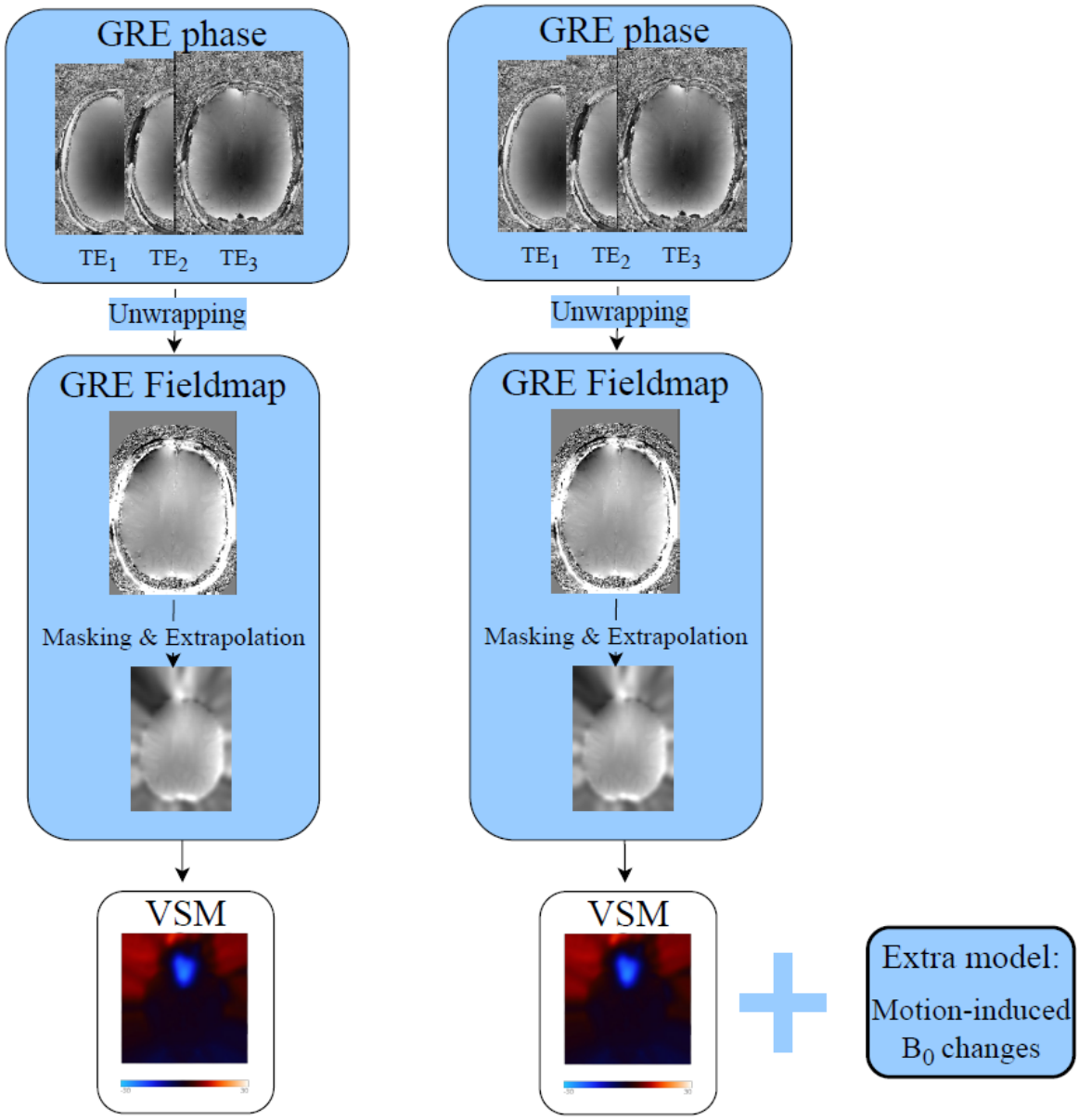

(a) Pipeline 1 (b) Pipeline 2

Figure 2.2: Static field mapping with GRE: Pipeline 1 (left) and Pipeline 2 (right) with the additional motion model

distortion of the same magnitude but in opposite directions. The model developed by (Andersson et al. 2003) tries to estimate the fieldmap $\Delta\omega_0$ by minimizing the difference between the blip-up and blip-down images. The following problem is being solved by this method:

$$\begin{bmatrix}\mathbf{f}_+\\ \mathbf{f}_-\end{bmatrix} = \begin{bmatrix}\mathbf{K}_+\\ \mathbf{K}_-\end{bmatrix}\rho \tag{2.3}$$

where ρ is the true image, $\mathbf{f}_+/\mathbf{f}_-$ are the distorted blip-up/blip-down images and $\mathbf{K}_+/\mathbf{K}_-$ are real-valued square matrices that map the pixel locations in the true image to the distorted image. Therefore, $\mathbf{K}_+/\mathbf{K}_-$ represent the same displacement field but in opposite direction. If the image was undistorted, these matrices would both be unity. SCOPE method estimates $\mathbf{K}_+/\mathbf{K}_-$ by solving Equation 2.3 using regularization in an iterative process, since the problem is ill-posed

Implementation

The pipeline of this method can be seen in Figure 2.3. First, SPM12's [22] new tool SCOPE (Susceptibility Correction using Opposite PE), is used to estimate the fieldmap based on the theoretical model introduced in 2.1.2. If multiple blip-up/down volumes are given to SPM12, they are realigned and the mean blip-up/down volume are used to compute the fieldmap. This fieldmap $\Delta\omega_0$ is then used to compute one unique VSM and unwarp distorted EPI data.

SDC SCOPE

As in the case of SDC GRE, the fieldmap obtained from SCOPE is a basis for two unwarping pipelines. In the first pipeline, a simultaneous motion and distortion correction is performed, but dynamic field changes are ignored, as described in 2.1.1.

SDC SCOPE + motion model

In the fourth pipeline, distorted data is unwarped using SPM12 *"Realign & Unwarp"*. As in 2.1.1, the correction is therefore accounting for the susceptibility-by-motion interaction modeling dynamic field changes due to motion.

2.1.3 DDC with GRE reference

Theory

To obtain a fieldmap for each volume, this method uses the phase of the EPI data. As stated in Section 1.1.4, the phase signal φ of MRI consist of a component proportional to the fieldmap $\Delta\omega_0$ and a phase offset φ_0:

$$\varphi(x,y,z) = 2\pi\mathrm{TE}\cdot\underbrace{\Delta\omega_0(x,y,z)}_{\text{Fieldmap}} + \underbrace{\varphi_0(x,y,z)}_{\text{Phase offset}}$$

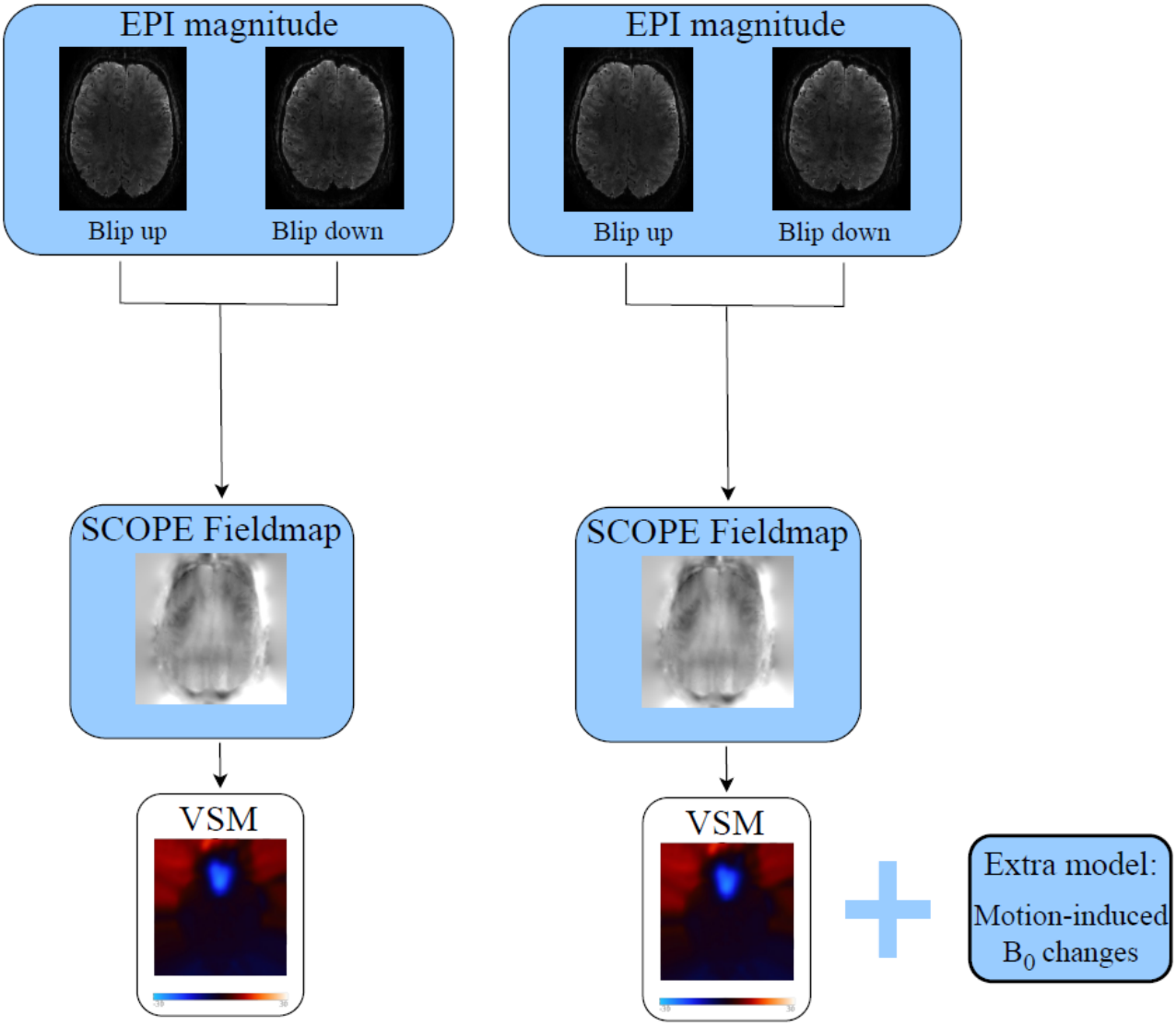

(a) Pipeline 3

(b) Pipeline 4

Figure 2.3: Static field mapping with SCOPE: Pipeline 3 (left) and Pipeline 4 (right) with the additional motion model

A first reference fieldmap is obtained from phase data of preliminary GRE scans at multiple TEs, as in the 1^{st} pipeline:

$$\Delta\omega_0^{\text{ref}} = \frac{\varphi_{\text{TE}_2} - \varphi_{\text{TE}_1}}{2\pi(\text{TE}_2 - \text{TE}_1)} = \frac{\Delta\varphi}{2\pi\Delta\text{TE}}$$

Then, instead of using this fieldmap to unwarp the distorted data, it is used to estimate the value of the phase offset φ_0. If we assume that the field inhomogeneities do not change between the reference GRE scan and the first EPI time point (tp=1), we have:

$$\Delta\omega_0^{\text{ref}} = \Delta\omega_0^{\text{fMRI}}(\text{tp=1}) = \frac{\varphi_{\text{tp=1}}^{\text{fMRI}} - \varphi_0}{2\pi\text{TE}} \tag{2.4}$$

From this equation, we are able to estimate the phase offset φ_0:

$$\varphi_0 = \varphi_{\text{tp=1}}^{\text{fMRI}} - 2\pi\text{TE}\Delta\omega_0^{\text{ref}} \tag{2.5}$$

By assuming that the phase offset remains relatively constant over time and during motion as in (Dymerska et al. 2018), a fieldmap for every time point (tp=i) can be computed by subtracting the phase offset from the EPI phase data $\varphi_{\text{tp=i}}^{\text{fMRI}}$:

$$\Delta\omega_0^{\text{fMRI}}(\text{tp=i}) = \frac{\varphi_{\text{tp=i}}^{\text{fMRI}} - \varphi_0}{2\pi\text{TE}} \tag{2.6}$$

A schematic of the theoretical method is depicted in Figure 2.4.

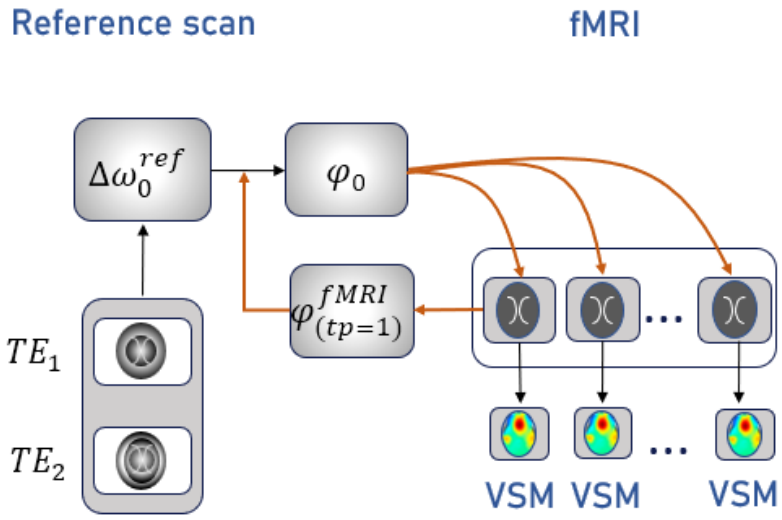

Figure 2.4: Graphical representation of the theoretical method of dynamic fieldmaps generation with phase offset subtraction: the reference fieldmap $\Delta\omega_0$ is obtained from GRE scans at two TEs and used with the phase of the EPI reference volume $\varphi_{(\text{tp=1})}^{\text{fMRI}}$ to estimate the phase offset φ. This phase offset is then subtracted from all EPI phase data to generate one VSM per volume.

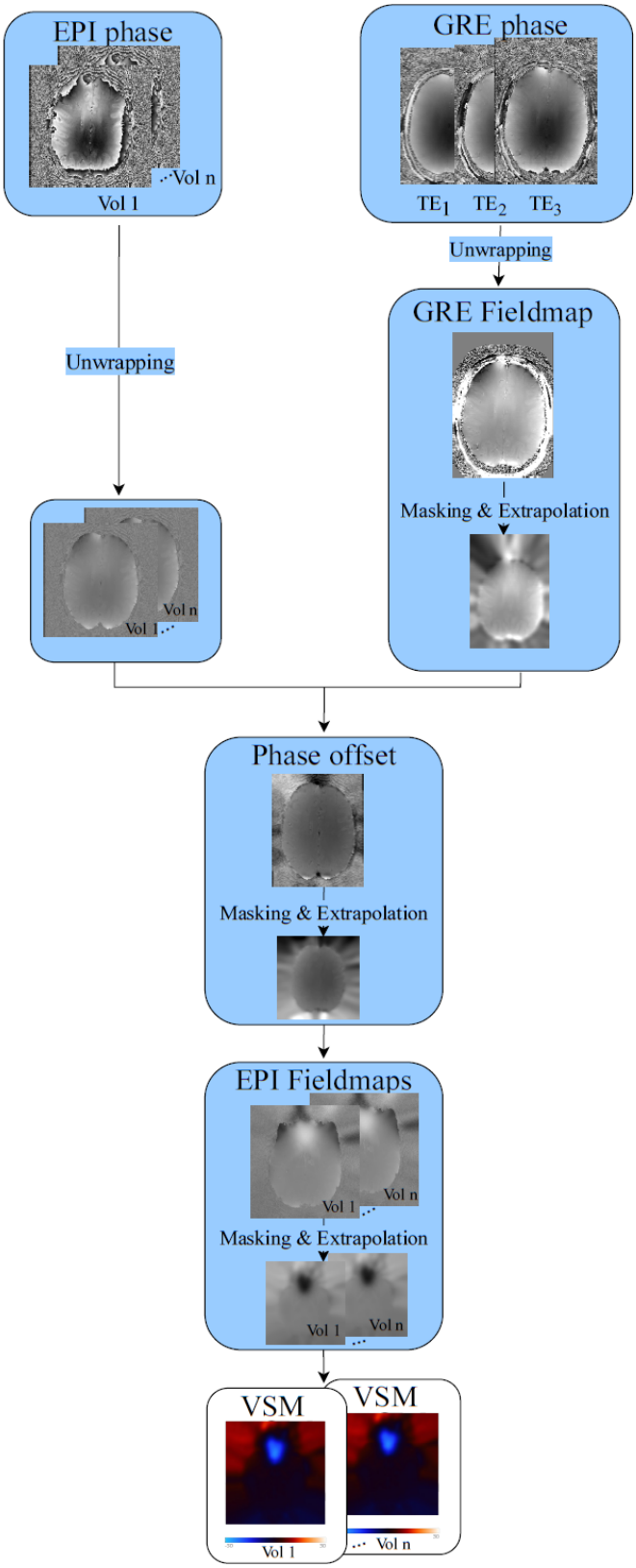

Figure 2.5: DDC with GRE reference (Pipeline 5)

Implementation

The complete pipeline diagram can be seen in Figure 2.5. As in the 1^{st} and 2^{nd} pipelines, the phase of the GRE scan at all TEs is unwrapped with ROMEO unwrapping tool [24] and the $\Delta\omega_0^{\text{ref}}$ fieldmap is directly extracted. This fieldmap is masked using an ICV mask as in Section 2.1.1 and then smoothed and extrapolated outside the brain boundaries with *"smoothn.m"*[25]. Finally, this reference fieldmap $\Delta\omega_0^{\text{ref}}$ is corregistered to the EPI space using SPM12.

In parallel, the phase data of all EPI volumes is also unwrapped using ROMEO [24]. Blip-up and blip-down data are unwrapped separately within two different ICV masks generated from probability maps of SPM12 segmentation tool. EPI phase volumes are unwrapped individually, meaning each EPI phase volume is unwrapped separately rather than using one common template for all time points.

After unwrapping the EPI phase data, the phase offset is computed using the GRE fieldmap and the phase data of the reference EPI volume as in Equation 2.5. This phase offset $\Delta\varphi_0$ is then masked with SPM12 segmentation tool and then smoothed and extrapolated outside the brain boundaries with *"smoothn.m"* from D. Garcia[25].

Thenceforth, the phase offset is subtracted from the phase of each EPI volume as in Equation 2.6 to obtain an EPI fieldmap for every time point. Finally, these series of EPI fieldmaps are masked using SPM12 segmentation tool, then smoothed and extrapolated with *"smoothn.m"*[25] before being converted into a VSM with Equation 2.1.

To unwarp EPI magnitude data, the same process as the one depicted in Section 2.1.1 is used. The EPI VSM is first added to the phase-encoding direction of a warp field. After that, motion correction is applied by multiplying this warp field by the rigid-body transformation matrix from each volume to the reference volume estimated with *"Realign (Estimate)"* from SPM12. Finally, through a single-step interpolation, the undistorted and motion corrected image is obtained for each volume.

2.1.4 DDC with SCOPE reference

Theory

This method can be seen as a combined technique. It uses the exact same equations as the ones in 2.1.3 to obtain dynamic EPI fieldmaps, but the reference fieldmap $\Delta\omega_0^{\text{ref}}$ is estimated from the model using blip-up and blip-down EPI magnitude data as described before in Equation 2.3 [2].

Once the reference fieldmap has been estimated, it is subtracted from the phase data of the EPI reference volume to obtain the phase offset φ_0 (Equation 2.5). Then, dynamic fieldmaps $\Delta\omega_0^{\text{fMRI}}(\text{tp})$ can be extracted with Equation 2.6 to unwarp each time points individually.

This approach tries to only utilize the EPI sequence with embedded blip-reversed volumes, as well as the phase data for each of the EPI volumes. In contrary to the DDC

with GRE reference approach, this method would therefore not need any additional GRE scan to derive dynamic fieldmaps.

Implementation

The diagram of the complete pipeline can be seen in Figure 2.6. The reference fieldmap is obtained using the new SPM12 tool called SCOPE that takes blip-up and blip-down magnitude EPI volumes and try to minimize the difference between them. In parallel, the EPI phase data is unwrapped using ROMEO, as described in Section 2.1.3.

Then, the pipeline is exactly the same as for the previous dynamic distortion correction, as described in Section 2.1.3.

2.2 Data acquisition

In order to apply the different correction algorithms and to assess their robustness, MRI data was acquired. The data presented in this thesis were collected on three participants on a 7T Siemens TERRA (Siemens Healthcare, Erlangen, Germany) scanner using 8 transmit and 32-channel receive head coil (Nova Medical) at the Department of Imaging Neuroscience of University College London. All data were collected under local ethics agreement. This data can be divided in three experiments that are detailed in the following sections. The complete protocols for all experiments can be found in Appendix A. These measurements have included 3D EPI scans with protocols deployed for various studies at the department. Each protocol started with a "localizer" and a B_0 map acquired to allow for the definition and alignment of the scan plane, and the shimming of the scanner, respectively.

2.2.1 Experiment 1

A first set of data was taken retrospectively from another study and used to evaluate the performances of the different pipelines on a segmented EPI acquisition. In this experiment, high-resolution T_2*-weighted segmented GRE 3D EPI acquisition was used in contrary to non-segmented acquisition as in Experiment 2 and 3 (see Sections 2.2.2 and 2.2.3). Four volumes were collected at the beginning with reversed-PE polarity (PA direction) relative to the ongoing time series acquisition (AP direction). To avoid chemical shift artefacts arising from fat signal, a water-selective binomial excitation was used.

The 3D EPI run had the following parameters: matrix size=240 × 240, echo spacing=1.2 ms and readout bandwidth=947 Hz/pixel. With an acceleration factor of 4 in the PE direction and 2-in-plane segments, the effective echo spacing was $\frac{1.2}{8} = 0.15$ ms. This corresponds approximately to a bandwidth in the PE direction of:

$$BW_{\mathrm{PE}} = \frac{1}{\mathrm{ESP}_{\mathrm{eff}} \cdot M_{\mathrm{PE}}} = 27.78 \text{ Hz/pixel}$$

The detailed acquisition parameters can be seen in Table 2.1. The presence of a preliminary GRE scan allowed to use all the pipelines for distortion correction.

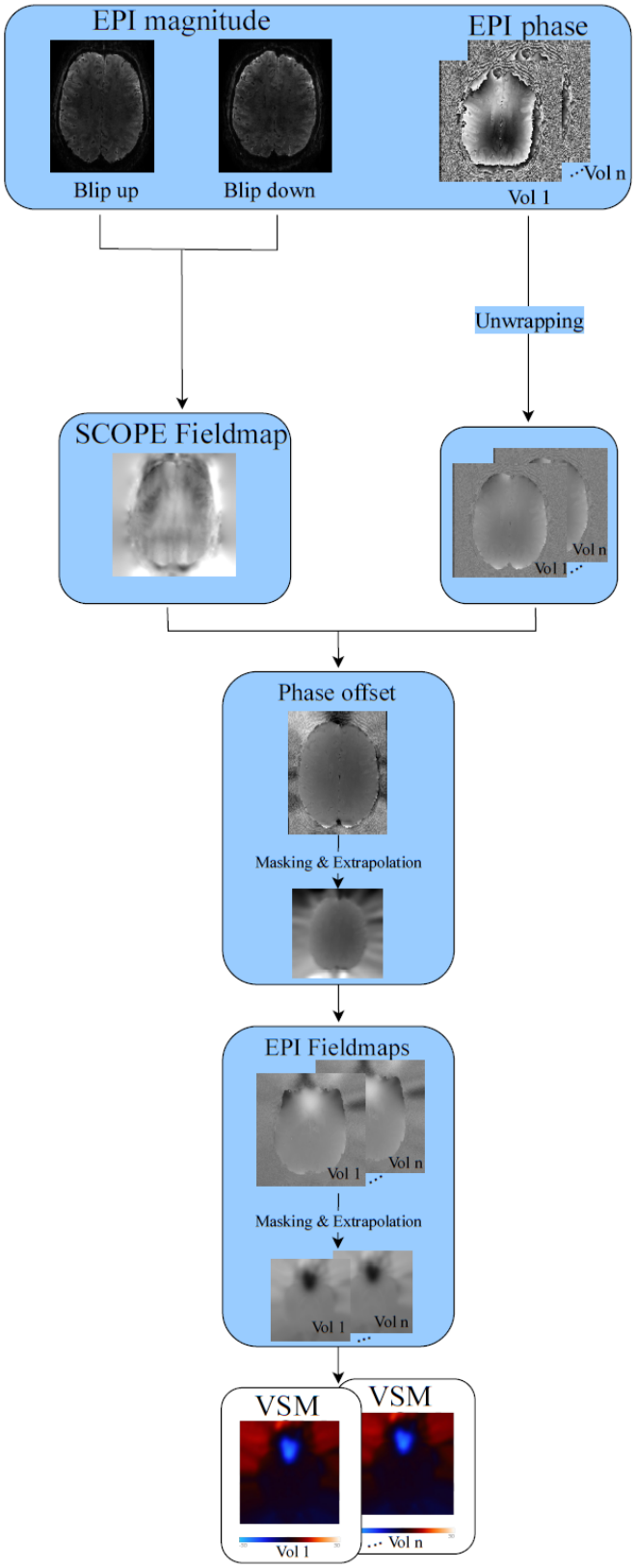

Figure 2.6: DDC with SCOPE reference (Pipeline 6)

Sequence	TE (ms)	TR (ms)	FA	Resolution (mm iso)	PF	Segments	Acceleration in PE1	Slices	Effective echo spacing (ms)
3D EPI	18.5	43.0	13°	0.8	6/8	2	4	88	0.15
GRE	[2.56:2.56:20.5]	25.0	24°	0.8	Off	-	2	192	-

Table 2.1: Data acquisition protocol for Experiment 1.

With an echo spacing divided by two due to segmentation, the phase has less time to accumulate and geometric distortion in the PE direction are less visible. As stated in Section 1.5.1, multi-shot EPI can be used to reduce the distortions due to B_0 inhomogeneities. However, in this project, the goal is to have those distortions and to correct for them in post-processing. With less distortion, the effect of the correction methods is less visible. Therefore, this dataset is not analysed in detail in the content of this thesis, but some results are still provided in Section 3.1 to be able to compare them with unsegmented ones.

The following experiments used unsegmented EPI data. By increasing the effective echo spacing, more distortion is visible and the effect of the different correction methods can be more easily analysed.

2.2.2 Experiment 2

In the second experiment, 8 fMRI runs were acquired on one subject for a neuroscientific study run at the department and these data were used retrospectively for this project under the agreement from the Principal Investigator of that study.

High-resolution unsegmented T_2^*-weighted GRE 3D EPI were acquired with partial brain coverage. In each of the 3D EPI acquisitions, the first four volumes were collected with reversed-PE polarity (Posterior-Anterior (PA) direction) relative to the ongoing time series acquisition (Anterior-Posterior (AP) direction). To avoid chemical shift artefacts arising from fat signal, as in experiment 1, a water-selective binomial excitation was used.

The 3D EPI runs had identical matrix sizes=240 × 240, echo spacing=1.2 ms and readout bandwidth=947 Hz/pixel as in experiment 1. With an acceleration factor of 4 in the PE direction, the effective echo spacing was 0.3 ms. This corresponds approximately to a bandwidth in the PE direction of:

$$BW_{\mathrm{PE}} = \frac{1}{\mathrm{ESP}_{\mathrm{eff}} \cdot M_{\mathrm{PE}}} = 13.89 \text{ Hz/pixel}$$

Table 2.2 summarizes the details of the imaging protocol. All imaging parameters were kept the same for every run. The number of volumes acquired per run were variable:

$$\text{Nb volumes/run} = [201; 35; 184; 200; 113; 113; 113; 118]$$

As only fMRI data was collected, pipelines 3, 4 and 6 were the only ones applicable in this experiment.

Sequence	TE (ms)	TR (ms)	FA	Resolution (mm iso)	PF	Segments	Acceleration in PE1	Slices	Effective echo spacing (ms)
3D EPI	26.08	68.0	15°	0.8	6/8	1	4	96	0.3

Table 2.2: Data acquisition protocol for Experiment 2.

2.2.3 Experiment 3

The third experiment was designed specifically for this research project and contains all data required to apply all 6 pipelines prepared. The exact same unsegmented GRE 3D EPI sequence as in experiment 2 has been used with asupplementary prior GRE sequence to be able to implement Pipelines 1,2 (2.1.1) and 5 (2.1.3). The details of the imaging protocol can be found in Table 2.3.

Three fMRI runs were performed with the exact same imaging parameters as in Experiment 2 and contained 74 volumes each. In those 3 runs, the participant was asked to perform different tasks. The first run was simply a control run where the volunteer was asked to lie as still as possible. After that, in the second run, the participant was asked to move both his hand from his side to his chin (without touching it) and then move it away with a regular pace. This task has been used to induce dynamic breathing-like changes of the B_0 field without head motion [27].

In the last run, the subject was asked to move his chin slowly towards his chest to induce susceptibility-by-motion interaction. However, due to the padding on the sides of his head, a progressive motion was difficult to perform. A substantial rapid movement was executed at the beginning of the acquisition, preventing the reconstruction algorithm to correctly reconstruct the data. Thereby, this run has been excluded from the analysis.

Sequence	TE (ms)	TR (ms)	FA	Resolution (mm iso)	PF	Segments	Acceleration in PE1	Slices	Effective echo spacing (ms)
3D EPI	26.08	68.0	15°	0.8	6/8	1	4	96	0.3
GRE	[2.56:2.56:20.5]	25.0	24°	0.8	Off	-	2	192	-

Table 2.3: Data acquisition protocol for Experiment 3.

2.3 Analysis methods

To assess the robustness of the methods and compare the correction pipelines, qualitative and quantitative assessments were performed, focusing mainly on the temporal stability of the corrected EPI time series.

2.3.1 Qualitative assessment

First of all, intermediate steps of the processing pipelines have been inspected to optimize the correction.

Unwrapping

As explained in the Section 2.1, the unwrapping of the phase of GRE and of EPI was done using the ROMEO tool [24]. Changing parameters of the unwrapping can lead to very different results. Intermediate checks of the unwrapped phase were performed to make sure of the correctness of this step.

For EPI phase data, using template unwrapping or individual unwrapping lead to very different correction results. Indeed, as the reference EPI volume is the first target scan, if a lot of motion happens during the time series, template unwrapping of the last volume could include noise and lead to unwrapping errors. In individual unwrapping, each volume is unwrapped individually and not based on a template generated from a reference unwrapped phase.

However, when each time point is unwrapped individually, differences of $n2\pi$ can occur and cause shifts in the PE direction between adjacent corrected volumes. By looking at this intermediate step, such differences were detected.

To avoid these, a correction for phase jumps between adjacent volumes has been implemented. This function computes the median value of the phase over all voxels of the reference EPI volume within an ICV mask. Then, after calculating the median of all other volumes, it checks if a $n2\pi$ difference occurs between the reference median and the current median. If a $n2\pi$ difference is detected, it is corrected. By doing so, all potential image shifts due to $n2\pi$ difference in the unwrapped phase are avoided.

Masking

Masking of the data is also a crucial step of the correction pipelines. By using a low binarizing threshold, the mask could be too large and include noise, shifting voxels from outside of the brain to the inside. But with a too high threshold, phase signal from tissue at the brain boundary could be missed, leading to less accurate correction in these regions.

The masking used in all pipelines relies on the SPM12 segmentation tool. White matter, grey matter and CSF probability maps are extracted from a magnitude image and then summed to form an Intra-cranial volume (ICV) probability map. A threshold is defined to turn this ICV probability map into a binary mask. For GRE mask, the value of the threshold is 0.5 whereas for EPI data it is 0.8. The choice of this threshold was done manually in an intermediate step, by looking at the mask overlaying the data to check if every relevant information was contained within it. Most brain tissue and as little noise as possible should be included.

Extrapolation

Finally, another important intermediate step to analyse was the extrapolation and smoothing of the data. As mentioned in Section 2.1, when the fieldmaps and the phase offset were extrapolated outside the brain boundaries, it was done using a discretized spline smoother *smoothn.m* function by D. Garcia [25]. This robust smoothing process minimizes the influence of outlying data. The background values were padded with NaNs and thereby

treated as missing values, such that *smoothn.m* iteratively extrapolates values for these voxels based on a discrete cosine transform. By looking at the smoothed data, the smoothing parameter was determined such that it would smooth and extrapolate enough without loosing too much information.

Other smoothing methods could have been used, such as Gaussian smoothing or polynomial interpolation, but in the paper from (Dymerska et al. 2018), *smoothn.m* was established to work well for fieldmaps extrapolation. As MRI data can contain significant noise, a smoothing algorithm robust to outliers is really important. Moreover, it must have the ability to handle multidimensional data and missing values. *smoothn.m* provides a good balance between keeping important features and decreasing the noise.

2.3.2 Difference between blip reversed images

This analysis was done to assess the ability of each of the correction methods to remove differences between EPI volumes with blip up and down phase encoding direction, which are affected by the opposite distortions. Ideally, this difference should be minimised by an effective distortion correction method. To do that, the last blip up volume and the first blip down, which are the closest in time, are realigned. Then, the sum of the squared difference between them is calculated within an ICV mask:

$$\sum_{\text{voxels}} (x_{\text{up}} - x_{\text{down}})^2$$

with $x_{\text{up/down}}$, the voxel intensity of the blip up/down image.

A perfect correction should lead to a difference close to zero, as the blip up and down volumes are acquired very close in time. This would mean both blip up and blip down volumes would have been perfectly corrected and thereby very similar.

2.3.3 temporal Standard Deviation (tSTD)

This thesis focuses on comparison of geometric distortion correction method from a dynamic point of view. Temporal metrics are needed to analyse how the different methods behave dynamically. The first temporal metric used is the temporal standard deviation of the signal (tSTD), calculated voxel-wise from the entire EPI time series. It gives information about the temporal variability of the signal over time. High tSTD values indicate regions with substantial signal fluctuations, which can be due to distortions. A good distortion correction method should decrease the tSTD in distorted regions, indicating that the temporal variability has been reduced. This reduction in tSTD implies that the signal has become more stable over time.

Histograms

Local variations of the tSTD can be observed by looking directly at the maps. However, to summarize the analysis over a specific region of interest, histograms of tSTD were plotted. A tSTD histogram displays the distribution of temporal standard deviation

values across all voxels in the brain. In order to do that, the first step was to compute a mask from the mean corrected image in every pipeline. This was done using an ICV mask including white matter, grey matter and CSF generated as described in Section 2.3.1. Then, a common mask was generated by multiplying all the masks derived from the data corrected using various methods. Finally, histograms were computed from the tSTD maps within the common mask.

A very effective distortion correction method should shift the histogram towards lower tSTD values, indicating a reduction in temporal variability and noise. Moreover, a narrower histogram suggests more consistent signal variability across voxels. By examining the tails of the histograms, the proportion of voxels with very high tSTD values can be assessed. A good correction method should decrease the number of voxels with very high temporal variability.

High deformation in grey matter histograms

To observe regions where high deformations occur due to high off-resonance effects, another mask was used. First, the VSM from GRE fieldmap was thresholded to only have values of more than 2 voxels. This ensures to have a region of high distortion. Then, it was binarized and combined with a grey matter common mask. This combination of the two masks came from their intersection. In this case, only grey matter was chosen because usually in fMRI, the interest is about grey matter only. Finally, histograms of tSTD within this mask were plotted to see if stronger deformation regions lead to more visible differences between the methods.

2.3.4 temporal Signal-to-noise Ratio (tSNR)

Another well known temporal metric is the temporal signal-to-noise ratio (tSNR) of each voxel. It is the mean signal over time divided by the temporal standard deviation:

$$\text{tSNR} = \frac{\text{mean}}{\text{tSTD}}$$

This metric is relevant, because in fMRI, the % of signal change is of interest and tSNR is often used as a surrogate for BOLD-sensitivity estimation. In this project, tSNR shows if the distortion correction methods not only reduce the variability but also preserve the signal. A good correction method should improve tSNR by reducing the variability without significantly affecting the signal strength. Higher tSNR values indicate a better distortion correction method, with more consistent signal over time and low signal fluctuation due to distortion.

Chapter 3

Results

In this chapter, the results of the different correction methods are presented. First, temporal results from the segmented dataset are briefly shown. Then, the difference between blip-up and blip-down images is presented to assess the spatial accuracy of the various correction pipelines on unsegmented data. Finally, temporal metrics are depicted to investigate the temporal stability of the methods.

3.1 Segmented dataset

In the first experiment, the correction pipelines were applied to a segmented dataset. In this section, tSTD histograms of the corrected volumes are presented to see if substantial differences with respect to unsegmented data occurred.

By looking at the Figures 3.1 and 3.2, we observe that the static distortion corrections with no additional motion reach their peak for lower tSTD values. This is consistent with what is obtained with unsegmented datasets (see Section 3.3).

	SDC GRE	SDC GRE + motion model	SDC SCOPE	SDC SCOPE + motion model	DDC with GRE ref.	DDC with SCOPE ref.
Mean	44.81	47.61	44.77	48.58	46.34	46.27
Standard deviation	18.57	19.67	18.68	22.07	20.05	19.78

Table 3.1: Segmented EPI (experiment 1): mean and standard deviation of histograms

In Table 3.1, we observe that static corrections have the lowest mean variance and that dynamic distortion correction slightly increase the tSTD mean value, but not as much as the static correction with extra model motion. The exact same pattern is also found in the unsegmented datasets (see 2.2.2 2.2.3). However, the values are reduced for all correction methods compared to the one in both others experiments. In general, this dataset presents lower variance values. Therefore, in the next sections, only results from Experiment 2 and Experiment 3 are detailed.

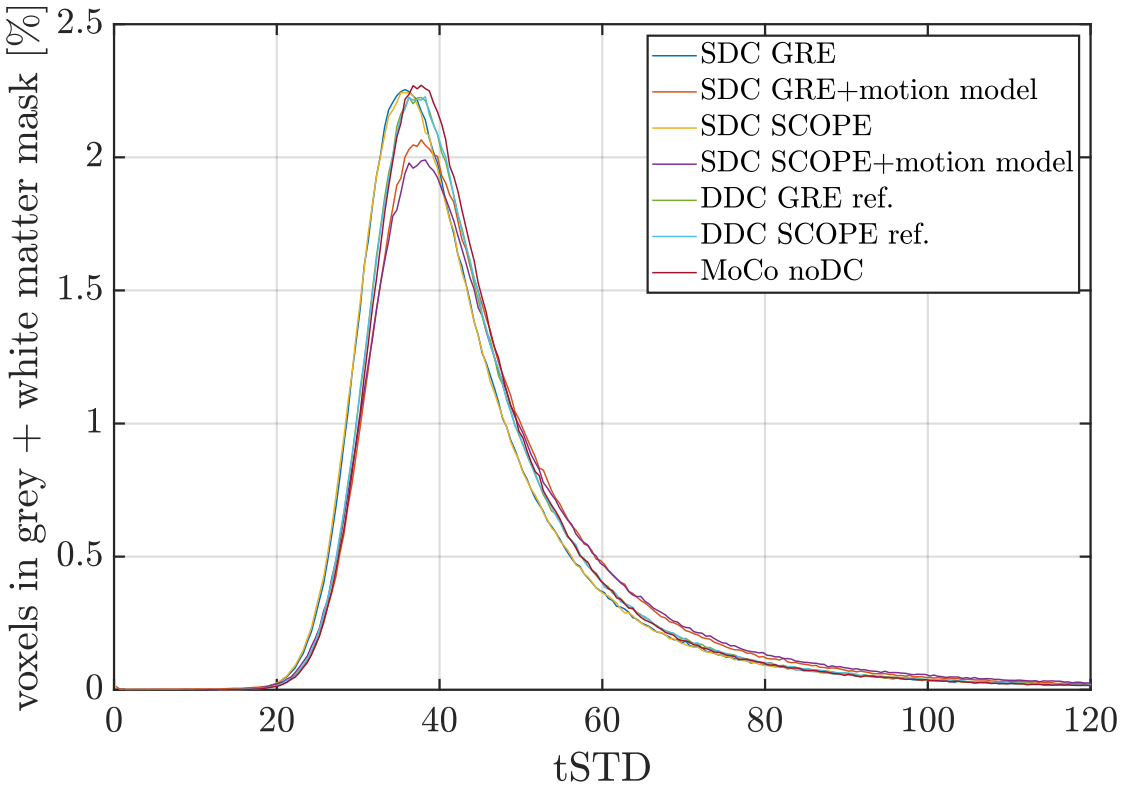

Figure 3.1: Segmented EPI (experiment 1) : tSTD histogram

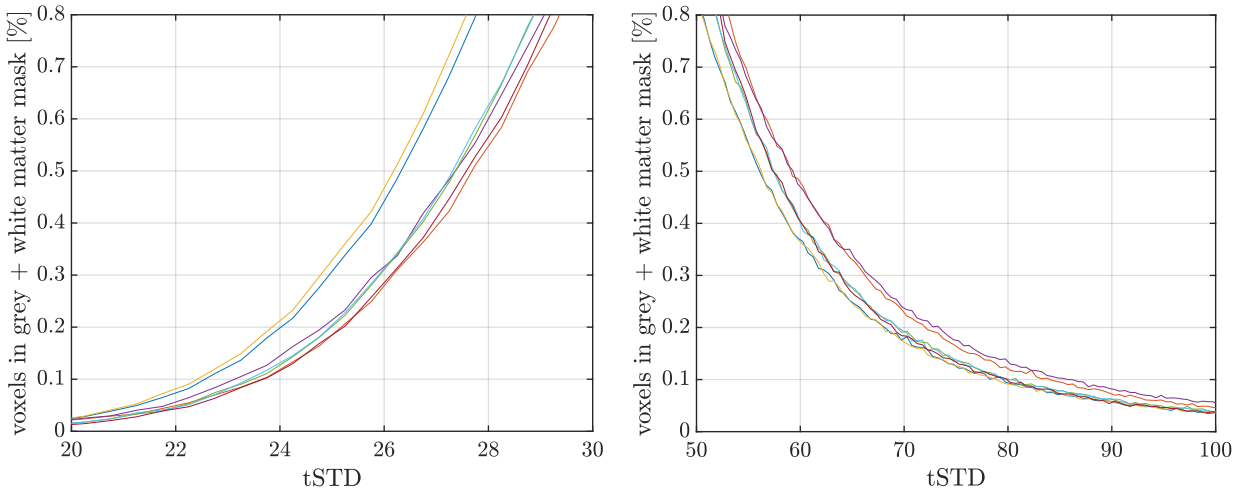

Figure 3.2: Segmented EPI (experiment 1): zooms of the plot 3.1

3.2 Difference between blip-reversed images

The difference between images acquired with opposite PE direction for all fMRI runs of Experiment 2 and 3 are presented in Figure 3.3.

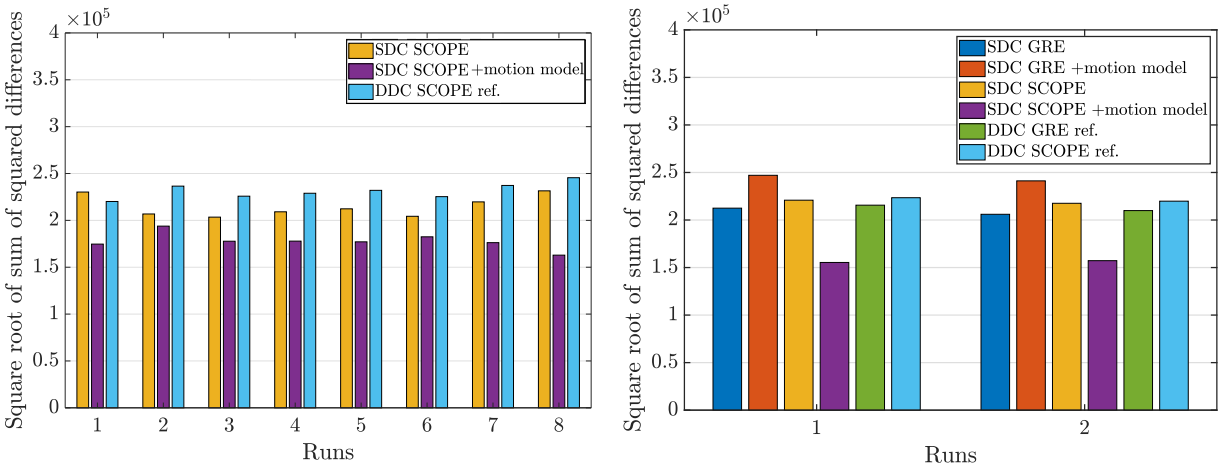

Figure 3.3: Square root of sum of squared difference between blip-up and blip-down EPI images from Experiment 2 (left) and 3 (right)

In these bar plots, it is evident that in each run of each experiment, "SDC SCOPE + motion model", including the additional modelling of B_0 changes due to motion, removes spatial differences between blip up and down volumes most effectively. All other methods performed slightly worse than "SDC SCOPE + motion model". For SCOPE-based approaches (dynamic and static) this observation was consistent for all 8 functional runs analysed.

3.3 tSTD histograms

Data were collected on two different subjects with respectively eight, and three fMRI runs. Results of three representative runs are shown below. Two EPI runs from the second experiment were chosen with more or less head motion. Then in experiment 3, only the run with the chin approaching task is shown. As explained in Section 2.2.3, the run with intentional motion had been excluded due to a very important initial movement preventing a good image reconstruction. Other than this run with large intentional motion with poor image quality, all results from all runs are consistent with what is presented in those three runs.

In the following Figures, results of EPI volumes that have been motion corrected but not distortion corrected (MoCo noDC) are also presented as a control case.

3.3.1 Experiment 2

The motion parameters of both fMRI runs from experiment 2 are plotted in Figure 3.4. We can see submillimetric motion in the first one. In the second run, the motion parameters are slightly increased, but they are still relatively low.

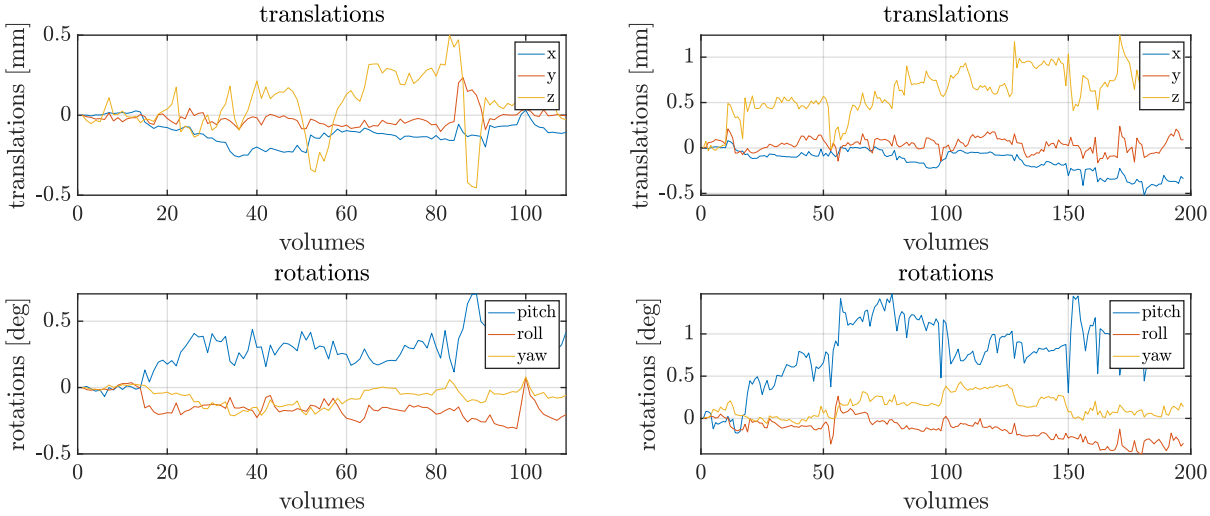

Figure 3.4: Motion parameters of 2 EPI runs of experiment 2: one with very **low** motion (left) and one with a little **more** motion (right)

When looking at the tSTD histograms in Figures 3.5,3.7, we see that, in general, using "SDC SCOPE" with no modelling of B_0 changes due to motion yields results with the highest temporal stability: the peak is reached for smaller tSTD than in other distortion correction methods. By looking at the zooms in Figure 3.6 and Figure 3.8, we clearly see that "SDC SCOPE" (in yellow) has more voxels with low tSTD values and the tail is shifted to the left.

By looking at the "DDC with SCOPE reference" results, we see that the peak is reached for higher tSTD values, but the tail is similar. This means that there aren't more high (>50) tSTD values.

In the case with low motion (Figures 3.53.6), the correction "SDC SCOPE + motion model" has increased tSTD globally, showing a shift of the peak value towards the peak with only motion correction. This histogram peak is also lower, showing a larger right tail (with high tSTD values) than any other distortion correction method.

When motion of the subject increases (Figure 3.7 3.8), "SDC SCOPE + motion model" has more similar tSTD characteristic to "SDC SCOPE", but it still shows lesser temporal stability (see Figure 3.8 left tail of the histogram).

In Tables 3.2 and 3.3, we observe that in both runs, "SDC SCOPE" has the lowest mean tSTD. When analysing the standard deviation of the histograms distributions, we see that "SDC SCOPE" is slightly higher than "DDC with SCOPE reference". This means that the variability is more uniform with the dynamic correction. When the subject head motion

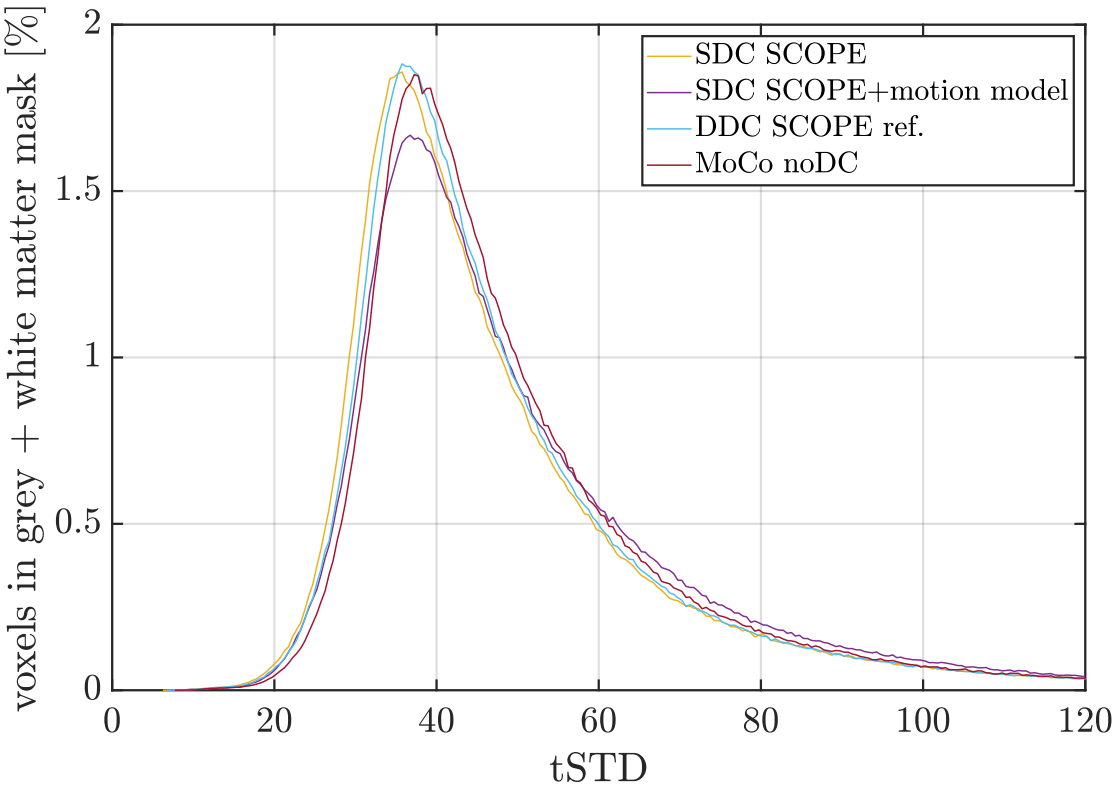

Figure 3.5: **Low** motion case (experiment 2): tSTD histogram

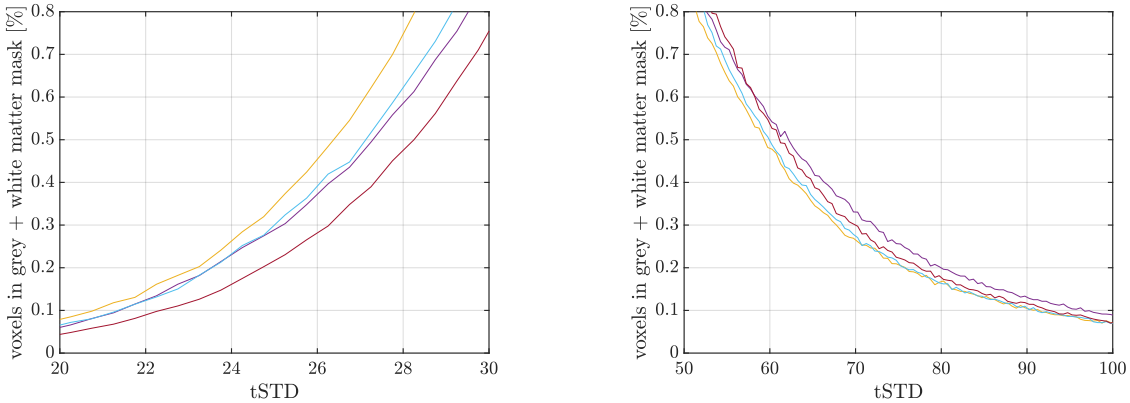

Figure 3.6: **Low** motion case (experiment 2): zooms of the plot 3.5

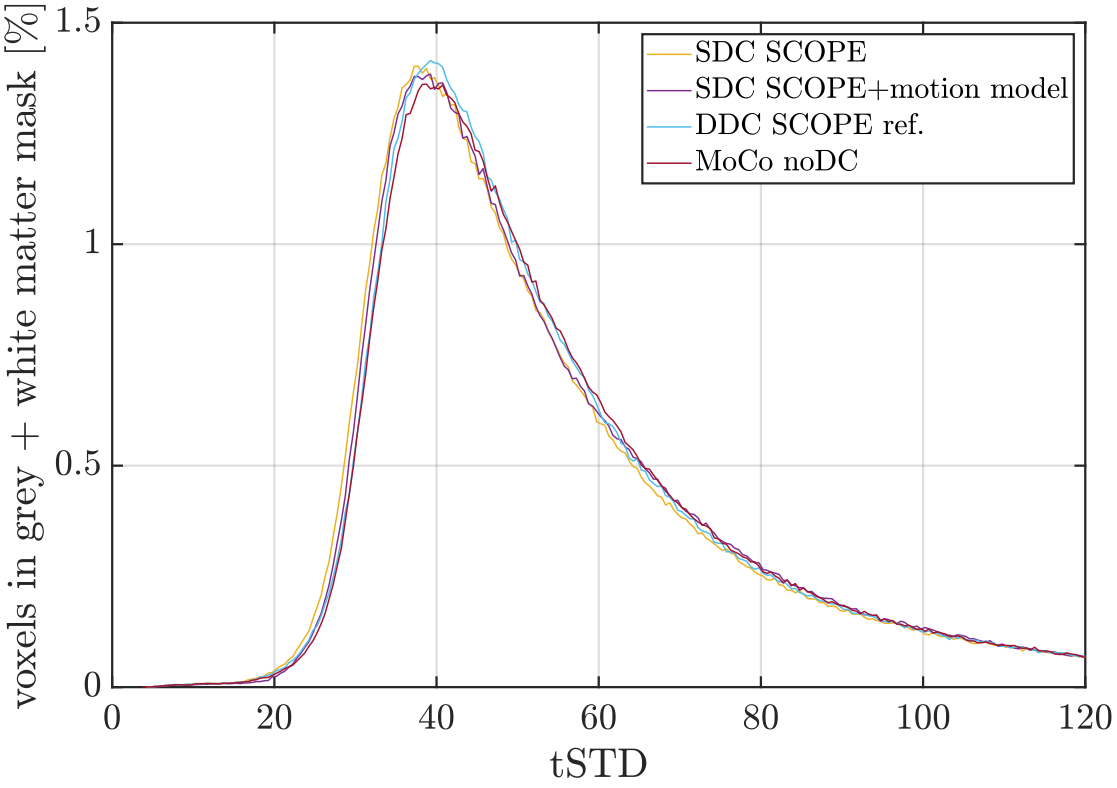

Figure 3.7: **More** motion case (experiment 2): tSTD histogram

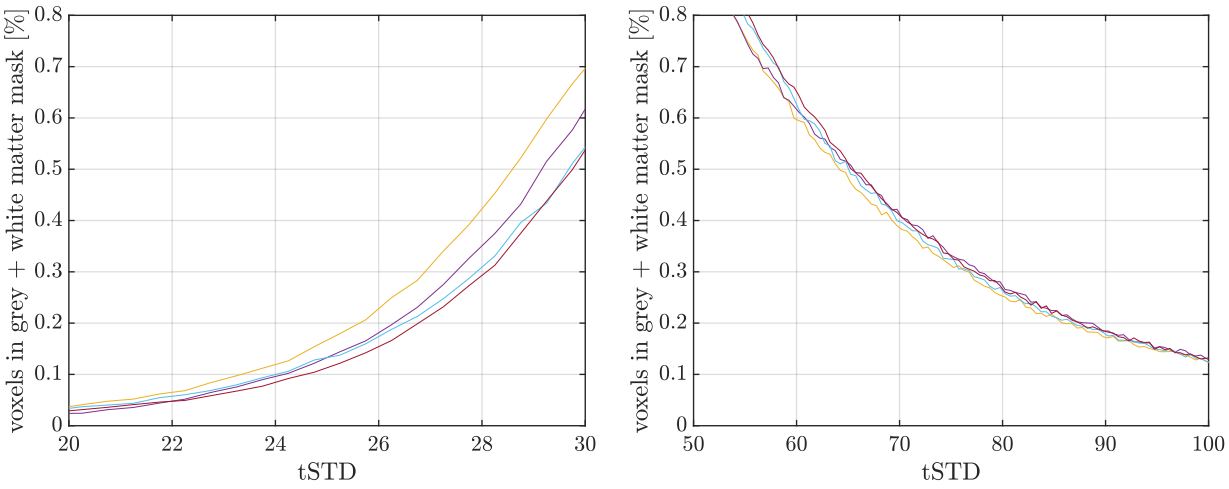

Figure 3.8: **More** motion case (experiment 2): zooms of the plot 3.7

increases, we also see that the mean tSTD of "SDC SCOPE + motion model" gets shifted to values closer to "SDC SCOPE". However, all the values are very close and comparable.

	SDC SCOPE	SDC SCOPE + motion model	DDC with SCOPE ref.
Mean	49.42	52.26	49.96
Standard deviation	24.60	25.76	24.31

Table 3.2: **Low** motion case (experiment 2): mean and standard deviation of histograms

	SDC SCOPE	SDC SCOPE + motion model	DDC with SCOPE ref.
Mean	58.63	59.16	59.35
Standard deviation	32.98	32.08	32.69

Table 3.3: **More** motion case (experiment 2): mean and standard deviation of histograms

3.3.2 Experiment 3

The motion parameters of the EPI run with the chin approaching task can be seen in Figure 3.9. These parameters are very low along the entire time series.

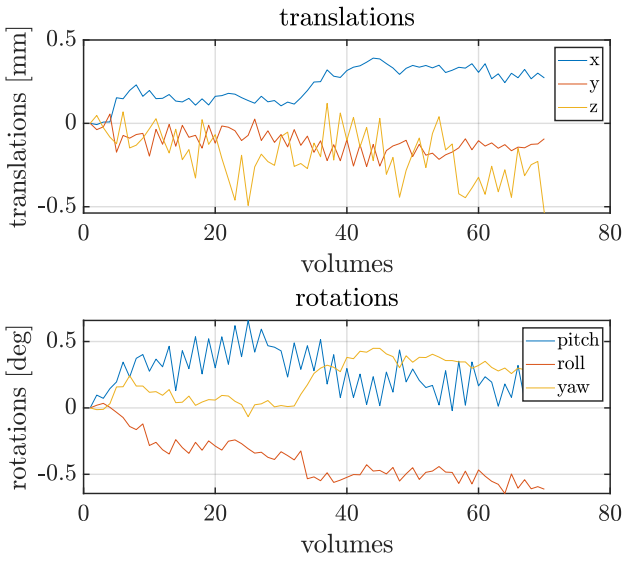

Figure 3.9: Motion parameters of chin task EPI runs of experiment 3.

The tSTD histogram of this experiment can be observed in Figure 3.10. The results for the pipelines 3,4 and 6 are consistent and similar to what we observed in experiment 2. "SDC SCOPE" has the peak with lowest tSTD values, whereas "SDC SCOPE +motion model" has the bigger right tail with more voxels having high tSTD values (Figure 3.11: right).

In the additional pipelines using preliminary GRE scan, "SDC GRE" follows the same trend as "SDC SCOPE". Both dynamic methods ("DDC with GRE reference" and "DDC with SCOPE reference") show very similar behaviour with tSTD histogram peak values and right tail values falling in between "SDC SCOPE"/"SDC GRE" and "SDC SCOPE +motion model"/"SDC GRE +motion model".

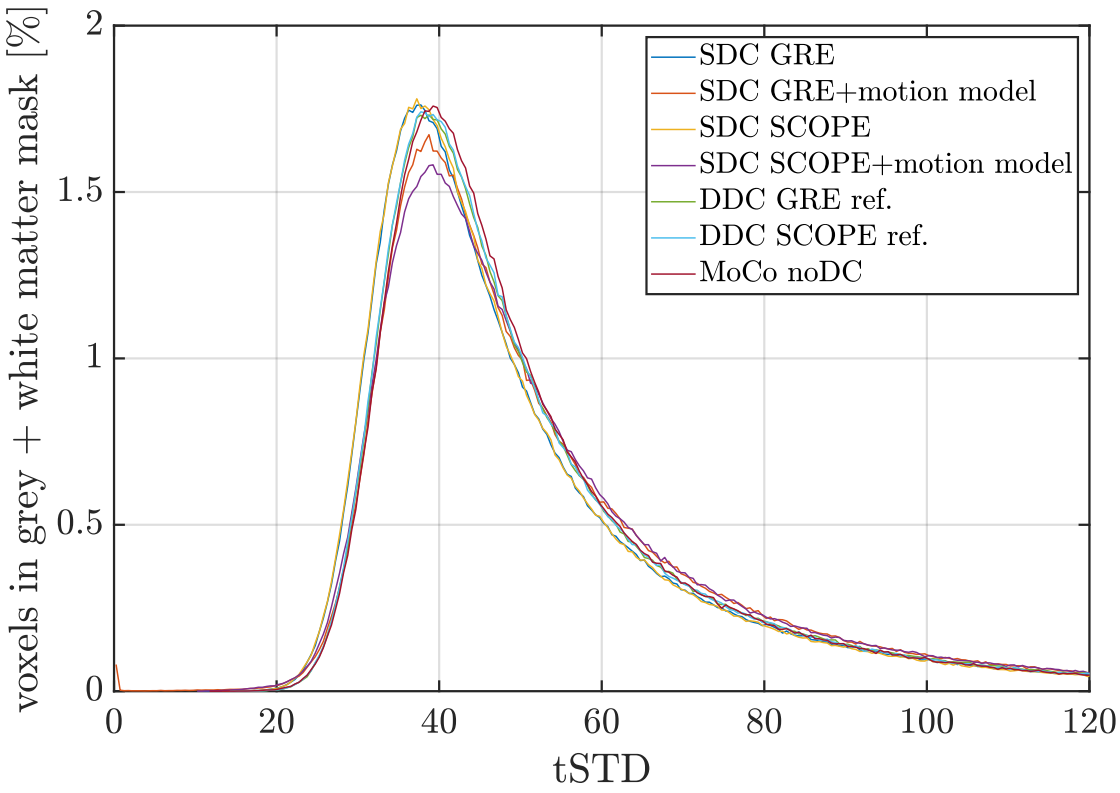

Figure 3.10: Chin task (experiment 3): tSTD histogram

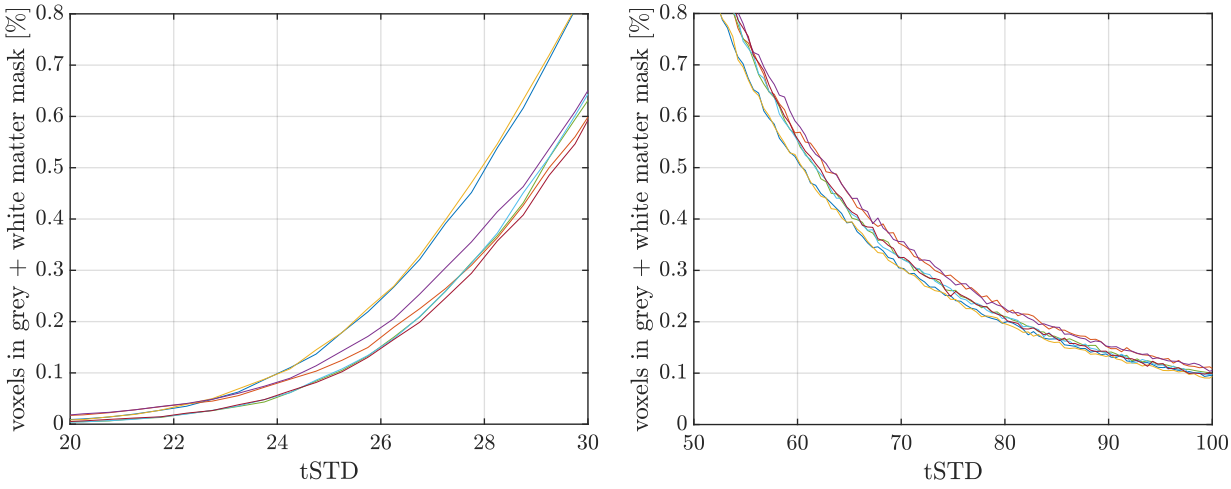

Figure 3.11: Chin task (experiment 3): zooms of the plot 3.10

	SDC GRE	SDC GRE + motion model	SDC SCOPE	SDC SCOPE + motion model	DDC with GRE ref.	DDC with SCOPE ref.
Mean	54.22	56.39	53.81	57.12	55.87	55.43
Standard deviation	30.41	30.27	29.90	32.27	31.48	30.74

Table 3.4: Chin task (experiment 3): mean and standard deviation of histograms

By looking at Table 3.4, we notice that "SDC SCOPE" has the best temporal stability with the lowest tSTD mean and standard deviation. Nevertheless, the greatest difference between tSTD of all the correction methods is around 6% which is relatively small.

For this experiment, another histogram has been computed only from regions in grey matter affected by distortions higher than 2 voxels, as explained in Section 2.3.3. The results that can be observed in Figures 3.12 and 3.13 and in Table 3.5, show consistency with the ones obtained with the whole brain tissue mask used before.

	SDC GRE	SDC GRE + motion model	SDC SCOPE	SDC SCOPE + motion model	DDC with GRE ref.	DDC with SCOPE ref.
Mean	58.80	61.99	58.37	61.94	60.72	60.28
Standard deviation	30.85	31.79	30.47	33.55	31.76	31.29

Table 3.5: Chin task (experiment 3) with high deformation and grey matter mask: mean and standard deviation of histograms

3.4 tSTD maps

The tSTD maps of the same fMRI runs as in the previous section are presented here. These maps allow for a more local analysis to determine which regions have been more or less impacted by the correction methods.

3.4.1 Experiment 2

The tSTD maps in Figure 3.14 correspond to the fMRI run with low motion parameters. Only small regional differences are visible for different correction methods, mostly at the brain boundaries or close to ventricles. We observe slightly lower standard deviation values in the white matter for "SDC SCOPE" than for the two other correction methods. However, with the dynamic correction ("DDC with SCOPE reference"), lower tSTD values are found in grey matter, especially in the occipital lobe (arrows 1 in Figure 3.14) and in the frontal region of the lateral ventricles (arrows 2 in Figure 3.14).

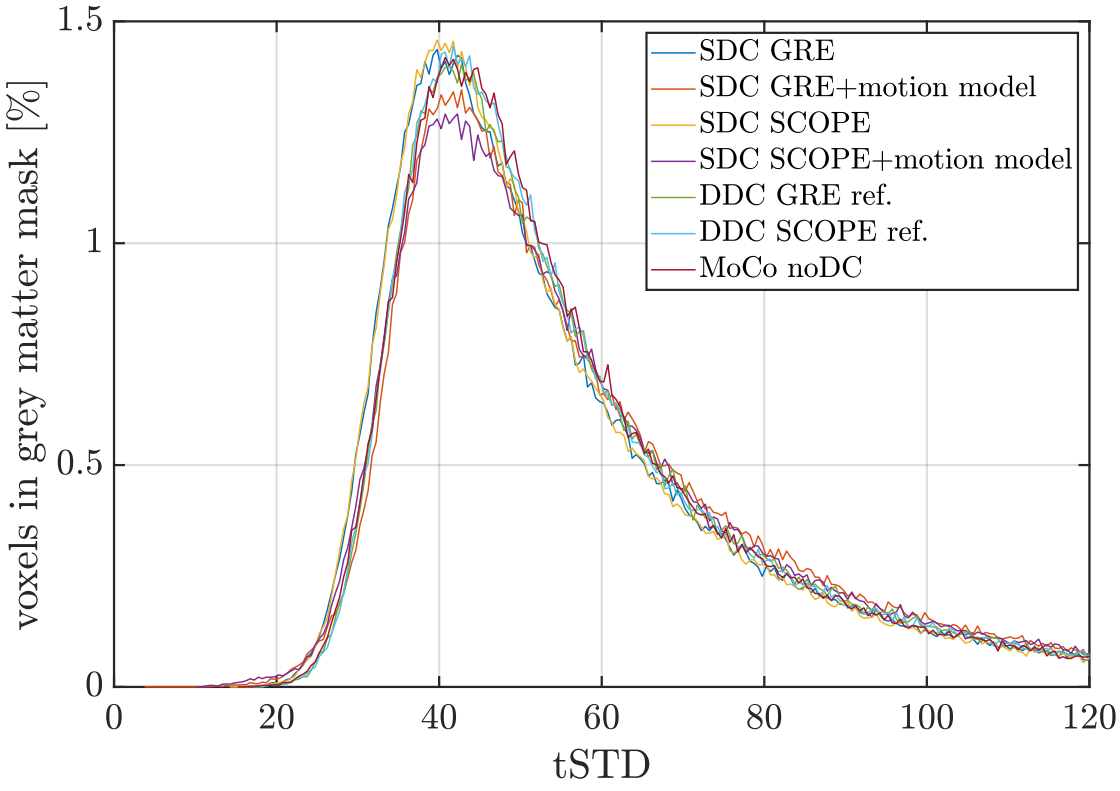

Figure 3.12: Chin task (experiment 3) with high deformation in grey matter mask: tSTD histogram

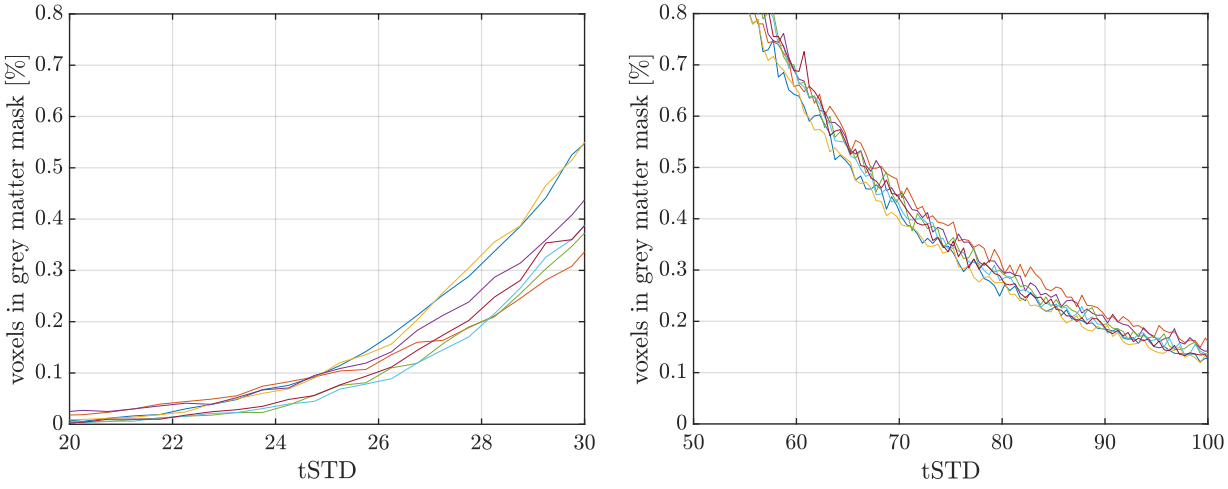

Figure 3.13: Chin task (experiment 3) with high deformation in grey matter mask: zooms of the plot 3.12

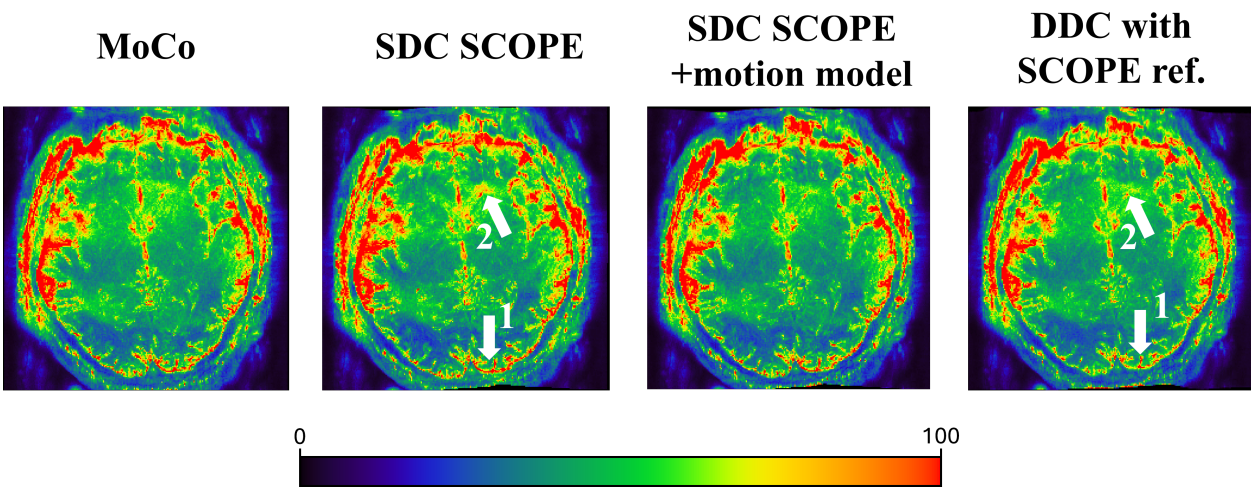

Figure 3.14: **Low** motion case (experiment 2): tSTD maps

In the run with more motion (Figure 3.15), less high tSTD values are seen using "SDC SCOPE + model motion" in the frontal region of the brain (arrow 1 in Figure 3.15), but higher tSTD values are visible close to the frontal horn of the lateral ventricle (arrow 2 in Figure 3.15). The rest of the results observed are consistent with what we saw before.

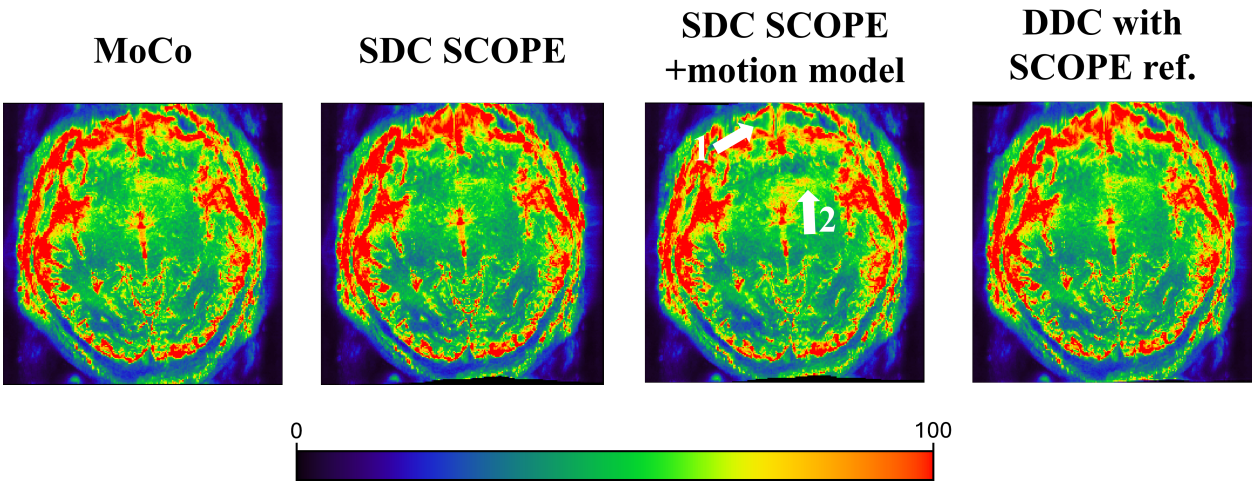

Figure 3.15: **More** motion case (experiment 2): tSTD maps

3.4.2 Experiment 3

The results of the chin approaching task from the second experiment can be seen in Figure 3.16. Everything looks consistent with what we observed in Experiment 1. In the static corrections ("SDC GRE" and "SDC SCOPE"), better stability is observed in white matter. Nevertheless, in grey matter, the use of dynamic distortion correction seems to reduce the standard deviation slightly.

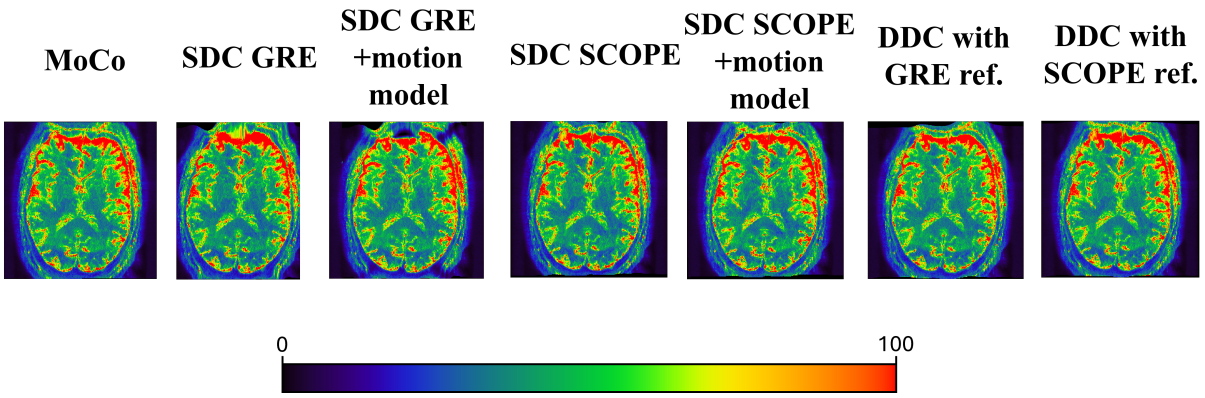

Figure 3.16: Chin task (experiment 3): tSTD maps

3.5 tSNR maps

Additionally, tSNR maps of the three representative runs are presented below. The slices shown in each run are the same as the ones in the tSTD maps.

3.5.1 Experiment 2

By looking at the tSNR results from the run with low motion in Figure 3.17, we can see slightly increased values in the occipital lobe with dynamic distortion correction ("DDC with SCOPE reference") with respect to the static field mapping methods. However, the rest of the results are quite similar across the pipelines.

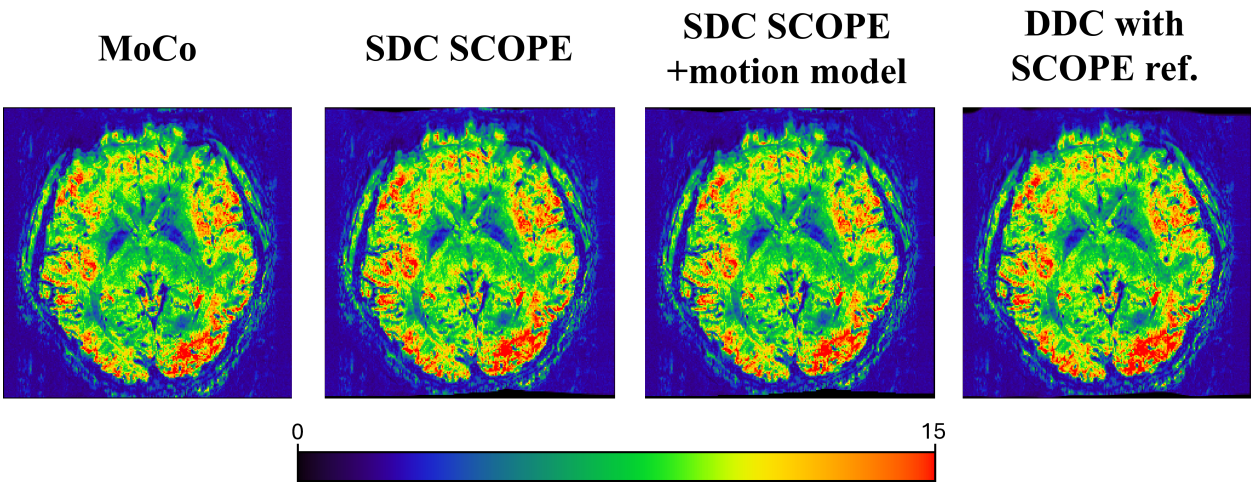

Figure 3.17: **Low** motion case (experiment 2): tSNR maps

In the case with more motion from experiment 2, the tSNR maps depicted in Figure 3.18 are relatively similar for all correction methods.

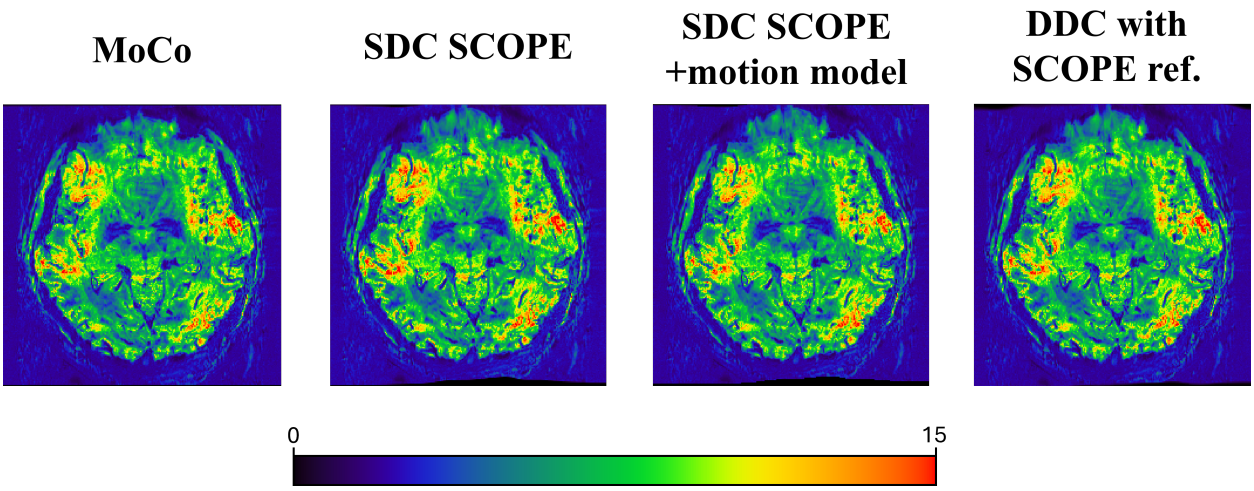

Figure 3.18: **More** motion case (experiment 2): tSNR maps

3.5.2 Experiment 3

Finally, the tSNR maps from the chin approaching task with every correction method are shown in Figure 3.19. Once again, no important difference between the methods can be seen from these results.

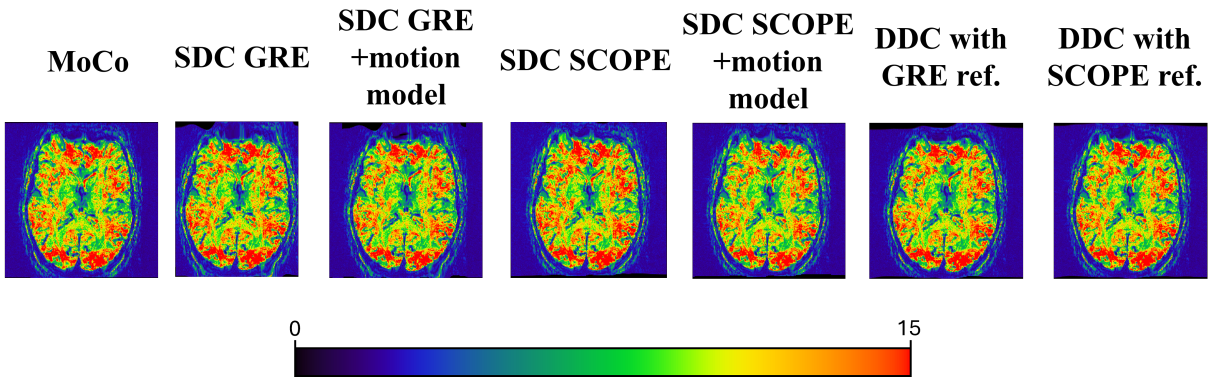

Figure 3.19: Chin task (experiment 3): tSNR maps

Chapter 4

Discussion

In this section, the results obtained will be discussed regarding the correction efficiency itself but also the temporal stability. The impact of the choice of the sequence as well as the task performed on the results will also be considered.

4.1 Correction efficiency

Because 'blip up' and 'blip down' EPI images have distortions in opposite directions, any difference between these images after correction can be a good indicator of how well a given method corrects distortions. The correction using "SDC SCOPE + motion model" provided the greatest similarity between blip-reversed volumes. This result was expected due to two main factors. Firstly, SCOPE fieldmap is generated by trying to minimize the difference between blip up and blip down images [2]. Therefore, any pipeline using a SCOPE fieldmap is expected to have better results than the ones using GRE fieldmap, which is acquired separately from EPI scan and any field changes between that scan and the target blip up and down volumes cannot be accounted for. However, the intermediate steps present in "DDC with SCOPE reference" pipeline (such as phase offset estimation and extrapolation) induce some extra variance in the corrected volumes. This leads to a higher difference between blip up and blip down volumes.

Another explanation for the improved results of the "SDC SCOPE + motion model" pipeline could be that by unwarping the data with SPM12 [22], Jacobian modulation is automatically applied. This method corrects for intensity variation caused by geometric distortion [26]. When voxels from the undistorted image get mapped to other locations in the distorted image, the signal change (compression or stretching) is taken into account. The Jacobian determinant indicates how much the volume of each voxel changes during this mapping. If the volume of a voxel is compressed, the Jacobian determinant will be less than one. On the other hand, if it is stretched, the determinant will be greater than one. To correct for the intensity variations, the signal intensity of the corrected image is multiplied by the local Jacobian determinant [28]. This Jacobian modulation therefore improves the similarity between blip-reversed volumes.

4.2 Temporal stability

By looking at the temporal standard deviation, we observe that static pipelines "SDC GRE" and "SDC SCOPE", which use exactly the same process to apply different fieldmaps, have strongly similar results. The same behaviour is also observed with the dynamic pipelines: "DDC with GRE reference" and "DDC with SCOPE reference". This suggests that both a SCOPE or a GRE fieldmap could be used to estimate the phase offset in the dynamic correction. Therefore, GRE preliminary reference scans are not mandatory to apply a dynamic correction. By using SCOPE, the reference scans are directly embedded in the fMRI sequence. Pipeline 6 ("DDC with SCOPE reference") enables to perform a distortion correction accounting for dynamic effects without needing any additional sequence. This is a considerable advantage given that in neurosciences studies, participants sometimes already spend a long time inside the scanner. In such way, we also avoid introducing errors (e.g. undesired shimming adjustments) between a reference scan and target EPI scan.

Overall, "SDC SCOPE" shows the best temporal stability. One of the potential reasons is that other methods introduce noise and therefore more temporal variance. The susceptibility-by-motion model [23] implemented in SPM12 and used in pipelines 2 and 4 increased temporal variance most from all the methods compared in this project. This could signify that this model is not appropriate for low motion cases. However, the choice of the sequence and the motion regime weren't ideal to obtain strongly visible differences between the correction methods.

4.3 Sequence choice

The EPI data analysed in this project came from accelerated 3D EPI. By accelerating the acquisition in the phase encoding direction, the geometric distortions are reduced. Therefore, the impact of the distortion correction methods is less visible than with non-accelerated data. Moreover, by using 3D EPI, the off-resonance effects are averaged over the entire volume acquisition, which can lead to image blurring rather than a distinctive voxel shifts creating a distorted image.

In the literature, non-accelerated 2D EPI is usually used to assess the efficiency of a dynamic distortion correction method [27]. The use of 2D EPI gives a snapshot of the breathing cycle per slice, inducing thereby more distinct dynamic changes within a slice and thus also distortions rather than blurring.

4.3.1 Segmented dataset

By using an EPI sequence with in-plan segments, the reduced effective echo spacing decreases the amount of distortion observed in the uncorrected image. Distortion correction still improves the data quality but to a lesser extent than with unsegmented data. The results presented in Section 3.1 show the same behaviour in terms of comparison between the methods. However, the temporal standard deviation values across all methods

are significantly lower than the ones obtained with unsegmented data. Since less distortion is present in this first experiment, the variance included in the initial data is reduced. Therefore, the mean tSTD values for all pipelines are smaller. For this reason, after analysing results from the first experiment, we decided to further investigate unsegmented EPI acquisitions to have a more visible effect.

4.4 Tasks

The tasks performed by the participant in the experiment 3 also had an impact on the results obtained. The tasks chosen are similar to the ones used in previous papers presenting the behaviour of dynamic distortion correction methods [27]. However, the results obtained in this project with these tasks do not show substantial differences between static and dynamic correction methods. Reasons for this will be explained in the following sections.

4.4.1 Chin approaching task pace

In Figure 4.1, we can see a screenshot of a frequency offset plot from EPI sequence navigators shown by the computer during the image reconstruction process of the fMRI run with the chin approaching task in experiment 2. It shows the change in frequency due to B_0 field inhomogeneities (y-axis) versus the repetition time (TRs) (x-axis). During this task, the participant moved his hands from his sides to close to his chin, then back to his sides with a regular pace. We clearly see from Figure 4.1 the constant pace of B_0 changes generated from this task. From this Figure, we would expect to have important dynamic B_0 field inhomogeneities along the time series. However, in the results presented in Section 3.3.2, dynamic distortion correction did not clearly improve the temporal metrics.

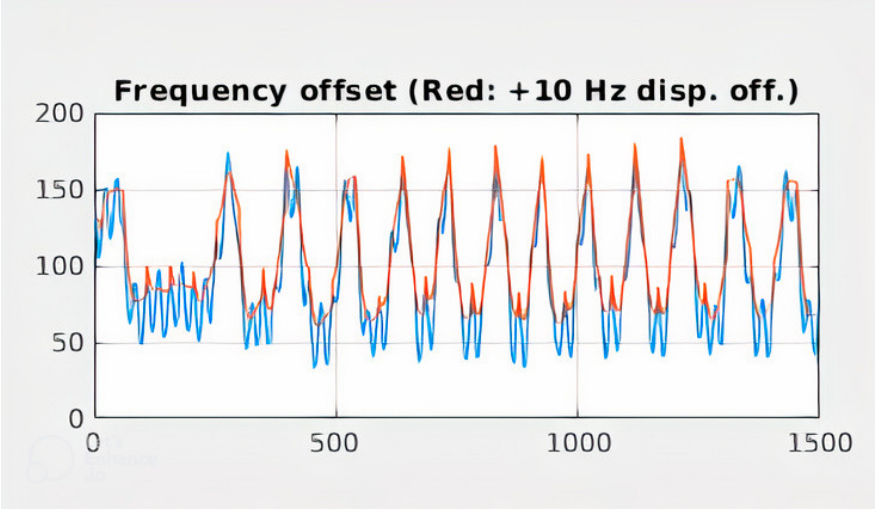

Figure 4.1: Screenshot of the reconstruction computer showing the change in frequency due to the chin approach task per repetition time.

To understand why such a variable field could be present in reality without impacting the reconstructed images, we need to compute the time over which 3D EPI averages the off-resonance effects. From Table 2.3, we can extract useful parameters of the 3D EPI sequence: the TR is 68ms, the number of slices is 96 and the acceleration factor in PE direction is 2. Therefore, we can compute the time needed to acquire one volume:

$$\frac{\text{TR} \cdot \text{nb}_{\text{slices}}}{\text{acceleration factor}} = \frac{68.10^{-3} \cdot 96}{2} = 3.264\text{s} \tag{4.1}$$

During this time, the off-resonance effects are averaged. We can then compute the period of the task from Figure 4.1. As said before, in this Figure, the x-axis represents the time in TR. This means that two points are separated by one TR. We observe five peaks happening during 500 TR. Thereby, the period of one chin approach task is:

$$\frac{500}{5} \cdot \text{TR} = 100 \cdot 68.10^{-3} = 6.8\text{s} \tag{4.2}$$

From Equation 4.1 and Equation 4.2, we notice that the off-resonance effect are averaged almost every half period of B_0 change:

$$6.8/3.264 = 2.083 \simeq 2$$

During a half period, we get +50Hz and -50Hz, therefore the B_0 dynamic changes are averaged to a value close to zero over a volume acquisition. This explains the lack of difference between the results obtained with static and dynamic distortion correction.

4.4.2 Low motion

The data from the second task consisting of moving the head towards the chest slowly was unusable, as explained in Section 2.2.3. Therefore, the data on which the corrections were applied had only very low head movement (<1.5mm translation and <1.5° rotation). Such a small motion did not allow testing various distortion correction methods in a regime where we would expect differences in temporal stability.

In the pipelines 2 and 4, the additional model accounting for susceptibility-by-motion changes is implemented in SPM12 [22] *"Realign & Unwarp"*. However, in SPM12 Manual [26], it is described that using this method with data containing little movement will provide no benefit. It only removes unwanted variance if the motion is above 1mm and 1°. In our results we not only observe no benefit from application of the additional motion model, we also see a slight deterioration of temporal stability when this model is applied. When head motion increases, the "SDC SCOPE + motion model" results become more similar to "SDC SCOPE" but still show slightly higher tSTD values.

Another impact of the low motion regime of our data is that we do not see a strong difference between static and dynamic distortion correction. Indeed, motion is known to modify the B_0 field along a time series. With variation of the static field across time, dynamic corrections should have reduced the temporal standard deviation. However, with such small head motion, its impact on the B_0 field across time was very weak, leading to small differences between dynamic and static correction methods.

4.5 Future work

Even if the correction pipelines seem to behave similarly in a small motion regime or for data with a periodic field changes (as in chin task), future work is desirable to test distortion correction temporal stability in other functional protocols and tasks. To be able to observe more clearly the differences between the methods, an unsegmented 2D EPI sequence with no acceleration could be acquired. If 3D EPI is still used, one could consider changing the pace of the chin approaching task in order to avoid the frequency averaging within one volume TR. Regarding the second task, a controlled head motion should be performed slowly towards the chest to see if it would show improved results of dynamic distortion correction. These experiments would be valuable for testing correction methods in extreme scenarios. This would allow researchers to choose the best method for a specific situation: while some functional tasks involve minimal head movement, others may have slow, sustained head drift over time. Rapid head movements are more common in tasks using virtual reality paradigms or pain stimulation. Additionally, by testing different correction methods within real neuroscientific studies, researchers can make more informed decisions about the optimal processing pipeline for their particular case taking into consideration temporal stability as well as functional activation.

Using this sequence and those tasks, differences between static and dynamic distortion correction methods will be more visible. Therefore, a more precise assessment will be possible. This will enable a choice between a simple static correction that does not account for the changes of B_0 along the time series or a dynamic correction which involves many intermediate steps that could increase the temporal variance if no substantial dynamic field changes are expected. One would expect that if the static field is highly variable during the acquisition, dynamic pipelines would reduce the temporal variance even considering all their intermediate steps.

Chapter 5

Conclusion

The growing trend in neuroscience research is to utilize functional magnetic resonance imaging (fMRI) at high (3T) and ultra-high (7T) magnetic field strengths. This is driven by the significant gains in signal-to-noise ratio (SNR), enabling researchers to acquire high-resolution functional maps, potentially even at the laminar level. However, fMRI typically employs fast imaging techniques like Echo-Planar Imaging (EPI) which are susceptible to geometric distortions caused by local field inhomogeneities. These inhomogeneities become increasingly pronounced at higher field strengths. To ensure accurate spatial localization of brain activation in 7T fMRI studies, robust correction methods for geometric distortions are essential.

In this thesis, different existing geometric distortion correction methods have been implemented and compared, focusing mainly on temporal stability. Additionally, a new dynamic distortion correction method has been developed and compared to existing methods. This technique does not require any preliminary scan and uses blip-reversed volumes to estimate the phase offset. Then, one fieldmap per time point is derived to account for any changes in the B_0 field along the time series.

The results showed that for 3D EPI and small motion ($<$1.5mm translation and $<1.5^\circ$ rotation), static distortion correction with a fieldmap generated from blip-reversed EPI volumes has the best temporal stability. In dynamic distortion correction, the intermediate computation steps induced some additional variance, which was not compensated by the reduction of variance occurring from accounting for the dynamic field changes.

However, the application of this new correction method on unsegmented 2D EPI could be very promising as off-resonance effects would not be average over the volume acquisition time. Further work is required to assess clearly the behaviour of each correction pipeline using 2D EPI.

Appendix A

MRI protocols

In the next pages, the PDF file of the protocols from experiment 2 and experiment 3 are presented with the detailed parameters used in the different sequences. Additional sequences than the ones presented in this thesis were present in the protocol are not shown, as they were used to providing data for other projects.

Only one fMRI sequence is shown because all runs from both Experiments were acquired using the exact same protocol.

\\USER\FIL Physics\Barbara\20240424_Katia_DDC\t1w_mfc_3dflash_v1k_0.8mm

TA: 6:16 PM: REF Voxel size: 0.8×0.8×0.8 mmPAT: 4 Rel. SNR: 1.00 : fl3d_1k

Properties

Prio recon	Off
Load images to viewer	On
Inline movie	Off
Auto store images	On
Load images to stamp segments	Off
Load images to graphic segments	Off
Auto open inline display	Off
Auto close inline display	Off
Start measurement without further preparation	Off
Wait for user to start	Off
Start measurements	Single measurement

Routine

Slab group	1
Slabs	1
Position	L0.0 A6.2 F21.1 mm
Orientation	Sagittal
Phase enc. dir.	A >> P
AutoAlign	---
Slice oversampling	0.0 %
Slices per slab	192
FoV read	256 mm
FoV phase	85.0 %
Slice thickness	0.80 mm
TR	25.00 ms
TE 1	2.56 ms
TE 2	5.12 ms
TE 3	7.68 ms
TE 4	10.24 ms
TE 5	12.8 ms
TE 6	15.4 ms
TE 7	17.9 ms
TE 8	20.5 ms
Concatenations	1
Filter	None
Coil elements	AC

Contrast - Common

TR	25.00 ms
TE 1	2.56 ms
TE 2	5.12 ms
TE 3	7.68 ms
TE 4	10.24 ms
TE 5	12.8 ms
TE 6	15.4 ms
TE 7	17.9 ms
TE 8	20.5 ms
MTC	Off
Flip angle	24 deg

Contrast - Dynamic

Reconstruction	Magnitude

Resolution - Common

FoV read	256 mm
FoV phase	85.0 %
Slice thickness	0.80 mm
Base resolution	320
Phase resolution	100 %

Resolution - Common

Slice resolution	100 %
Phase partial Fourier	Off
Slice partial Fourier	Off

Resolution - iPAT

PAT mode	GRAPPA
Accel. factor PE	2
Ref. lines PE	48
Accel. factor 3D	2
Ref. lines 3D	48
Reference scan mode	Integrated

Resolution - Filter Image

Image Filter	Off
Distortion Corr.	Off
Prescan Normalize	Off
Normalize	Off
B1 filter	Off

Resolution - Filter Rawdata

Raw filter	Off
Elliptical filter	Off

Geometry - Common

Slab group	1
Slabs	1
Position	L0.0 A6.2 F21.1 mm
Orientation	Sagittal
Phase enc. dir.	A >> P
Slice oversampling	0.0 %
Slices per slab	192
FoV read	256 mm
FoV phase	85.0 %
Slice thickness	0.80 mm
TR	25.00 ms
Concatenations	1

Geometry - AutoAlign

Slab group	1
Position	L0.0 A6.2 F21.1 mm
Orientation	Sagittal
Phase enc. dir.	A >> P
AutoAlign	---
Initial Position	L0.0 A6.2 F21.1
L	0.0 mm
A	6.2 mm
F	21.1 mm
Initial Rotation	0.00 deg
Initial Orientation	Sagittal

Geometry - Tim Planning Suite

Set-n-Go Protocol	Off
Table position	H
Table position	0 mm
Inline Composing	Off

System - Miscellaneous

Positioning mode	REF
Table position	H
Table position	0 mm

System - Miscellaneous

MSMA	S - C - T
Sagittal	R >> L
Coronal	A >> P
Transversal	F >> H
Coil Combine Mode	Sum of Squares
Save uncombined	Off
Matrix Optimization	Off
AutoAlign	---
Coil Select Mode	Default

System - Adjustments

B0 Shim mode	Advanced
B1 Shim mode	TrueForm
Confirm freq. adjustment	Off
Assume Dominant Fat	Off
Assume Silicone	Off
Adjustment Tolerance	Auto

System - Adjust Volume

! Position	L0.0 A1.8 F4.2 mm
! Orientation	T > C-15.0
! Rotation	-180.00 deg
! A >> P	192 mm
! R >> L	192 mm
! F >> H	71 mm
Reset	Off

System - pTx Volumes

B1 Shim mode	TrueForm

System - Tx/Rx

Frequency 1H	297.211698 MHz
Correction factor	1
Gain	High
Img. Scale Cor.	1.000
Reset	Off
? Ref. amplitude 1H	0.000 V

Sequence - Part 1

Dimension	3D
Elliptical scanning	Off
Contrasts	8
Bandwidth	434 Hz/Px

Sequence - Part 2

Gradient mode	Fast
RF spoiling	On

Sequence - Special

Noise Adjust	On
Reorder Object?	On
Partition Spoiler?	On
RF Spoiling Increment	144.0 Degrees
Trajectory	Lines in Partitions
Prewinder (PE, RO) Ramp	290 us
Prewinder (PE, RO) Dur.	610 us
Readout Ramp	110 us
Spoiler Ramp	240 us
MTC Spoil Ramp	200 us
MTC Spoil Flat	1000 us
RF Pulse Duration	240 us
Excitation	Non-Selective Rect
Reconstruction	Gadgetron

Sequence - Special

Bandwidth Time Product	6.0
No. of PI to Spoil	3.0 PI
Flip Angle of MTC pulse	180.0 Degrees
Num. CAIPI Partitions	228
Num. CAIPI Lines	282

Sequence - Assistant

Mode	Off

\\USER\FIL Physics\Barbara\20240424_Katia_DDC\nc_epi3d_v3s_1seg_96part_AP_121mono_320us_nomotion

TA: 5:01 PM: REF Voxel size: 0.8×0.8×0.8 mmPAT: 8 Rel. SNR: 1.00 : ep3dv3s

Properties

Prio recon	Off
Load images to viewer	On
Inline movie	Off
Auto store images	On
Load images to stamp segments	Off
Load images to graphic segments	Off
Auto open inline display	Off
Auto close inline display	Off
Start measurement without further preparation	Off
Wait for user to start	Off
Start measurements	Single measurement

Routine

Slab group	1
Slabs	1
Position	Isocenter
Orientation	T > C-15.0
Phase enc. dir.	P >> A
AutoAlign	---
Phase oversampling	0 %
Slice oversampling	0.0 %
Slices per slab	96
FoV read	192 mm
FoV phase	100.0 %
Slice thickness	0.80 mm
TR	68.00 ms
TE 1	26.08 ms
TE 2	300.00 ms
TE 3	300.00 ms
Filter	None
Coil elements	AC

Contrast - Common

TR	68.00 ms
TE 1	26.08 ms
TE 2	300.00 ms
TE 3	300.00 ms
MTC	Off
Flip angle	15.0 deg
Fat suppr.	Water excit. normal

Contrast - Dynamic

Reconstruction	Magnitude
Measurements	74
Pause after meas.	0.000 s

Resolution - Common

FoV read	192 mm
FoV phase	100.0 %
Slice thickness	0.80 mm
Base resolution	240
Phase resolution	100 %
Slice resolution	100 %
Phase partial Fourier	6/8

Resolution - iPAT

PAT mode	GRAPPA
Accel. factor PE	4

Resolution - iPAT

Ref. lines PE	112
Accel. factor 3D	2
Ref. lines 3D	96
Reference scan mode	GRE/separate

Resolution - Filter Image

Image Filter	Off
Distortion Corr.	Off
Prescan Normalize	Off
Normalize	Off
B1 filter	Off

Resolution - Filter Rawdata

Raw filter	Off
Elliptical filter	Off

Geometry - Common

Slab group	1
Slabs	1
Position	Isocenter
Orientation	T > C-15.0
Phase enc. dir.	P >> A
Slice oversampling	0.0 %
Slices per slab	96
FoV read	192 mm
FoV phase	100.0 %
Slice thickness	0.80 mm
TR	68.00 ms

Geometry - AutoAlign

Slab group	1
Position	Isocenter
Orientation	T > C-15.0
Phase enc. dir.	P >> A
AutoAlign	---
Initial Position	Isocenter
L	0.0 mm
P	0.0 mm
H	0.0 mm
Initial Rotation	180.00 deg
Initial Orientation	T > C
T > C	-15.0
> S	0.0

Geometry - Tim Planning Suite

Set-n-Go Protocol	Off
Table position	H
Table position	0 mm
Inline Composing	Off

System - Miscellaneous

Positioning mode	REF
Table position	H
Table position	0 mm
MSMA	S - C - T
Sagittal	R >> L
Coronal	A >> P
Transversal	F >> H
Coil Combine Mode	Sum of Squares

System - Miscellaneous

Save uncombined	Off
Matrix Optimization	Off
AutoAlign	---
Coil Select Mode	Default

System - Adjustments

B0 Shim mode	Advanced
B1 Shim mode	TrueForm
Confirm freq. adjustment	Off
Assume Dominant Fat	Off
Assume Silicone	Off
Adjustment Tolerance	Auto

System - Adjust Volume

Position	Isocenter
Orientation	T > C-15.0
Rotation	-180.00 deg
A >> P	192 mm
R >> L	192 mm
F >> H	77 mm
Reset	Off

System - pTx Volumes

B1 Shim mode	TrueForm

System - Tx/Rx

Frequency 1H	297.211698 MHz
Correction factor	1
Gain	High
Img. Scale Cor.	1.000
Reset	Off
? Ref. amplitude 1H	0.000 V

Sequence - Part 1

Dimension	3D
Contrasts	1
Bandwidth	947 Hz/Px

Sequence - Part 2

Gradient mode	Fast
RF spoiling	On

Sequence - Special

Caipi Delta	0
In-plane segments	1
Number of RF pulses	3
Sinc duration	320 us
TBWP	24
Phase Evolution	540 deg
Off resonance frequency	0 Hz
VoxDeph	1 2pi
SpoilAmp	20 mt/m
EddCurr0	0 us
EddCurr1	250 us
TRamp	210 usec
TFlat	800 usec
effective TE	26080 usec
Quiet File	None
SlabGradScale	15.0
IceProgram	IceProgram2DiPatOffline3D
Noise Adjust	On
RF Spoil Basic Inc	50.0 deg
Trigger Type	Vol3ms

Sequence - Special

X_Shim_0	0.0 mt/m*ms
X_Shim_1	0.0 mt/m*ms
X_Shim_2	0.0 mt/m*ms
Y_Shim_0	0.0 mt/m*ms
Y_Shim_1	0.0 mt/m*ms
Y_Shim_2	0.0 mt/m*ms
Z_Shim_0	0.0 mt/m*ms
Z_Shim_1	0.0 mt/m*ms
Z_Shim_2	0.0 mt/m*ms
RO_Off	Off
PE_Off	Off
RO_OnSlice	Off
PE_OnSlice	Off
RO_Opp	On
PE_Opp	On
BlipUP_DOWN	On
PCAutoCorr	Off
PCAcrossSeg	Off
OnlineFFT	On
PFSubMatrix	Off
PF_POCS	Off
DummyNavigators	Off
Navs always on	On
Navs on for ref scans	On
Lin Ref Part	On
Sym Ref Data	Off
Late PF	Off
FlyBack Exc	On
MT_GaussPulse	Off
MT_HardPulse	On
MT dual-Freq	Off
Part. enc. balanced in	On
Pol slice sel grad	Off
Dummies	10 AccVol
Fillers	0 AccVol
BlipUpDown	4 BlipVol
MT FlipAngle	220 Deg
MT OFFRES	2000 Hz
MT PLS_DUR	4000 us
MT-subpulse	10 Number
MT-subpulseFA	12 Deg
MT-subpulse_tau	100 us
m_lMT_HardPulse_Dur	200 us

Sequence - Assistant

Mode	Off

Bibliography

[1] P. Jezzard and R. S. Balaban. Correction for geometric distortion in echo planar images from B0 field variations. *Magnetic Resonance in Medicine*, 34(1):65–73, 1995. ISSN 1522-2594. doi: 10.1002/mrm.1910340111.

[2] J. L. Andersson, Stefan Skare, and John Ashburner. How to correct susceptibility distortions in spin-echo echo-planar images: application to diffusion tensor imaging. *NeuroImage*, 20(2):870–888, October 2003. ISSN 1053-8119. doi: 10.1016/S1053-8119(03)00336-7.

[3] JP. Marques and R. Bowtell. Evaluation of a new method to correct the effects of motion-induced b0-field variation during fmri. In *Proc 13th Annu Meet ISMRM*, 2005.

[4] F. Lamberton, N. Delcroix, D. Grenier, B. Mazoyer, and M. Joliot. A new EPI-based dynamic field mapping method: application to retrospective geometrical distortion corrections. *Journal of magnetic resonance imaging: JMRI*, 26(3):747–755, September 2007. ISSN 1053-1807. doi: 10.1002/jmri.21039.

[5] J. L. Prince and J. M. Links. *Medical imaging: Signals and Systems (2nd edition)*. Pearson, 2015.

[6] H. A. Sharma. MRI physics–basic principles. *Acta Neuropsychiatrica*, 21(4):200–201, August 2009. ISSN 0924-2708, 1601-5215. doi: 10.1111/j.1601-5215.2009.00404.x.

[7] C Phillips. Gbio0008-1: Medical imaging (slides). *Université de Liège*, 2022-2023.

[8] R. W. Brown, Y.-C. Norman Cheng, E. Mark Haacke, Michael R. Thompson, and R. Venkatesan. *Magnetic Resonance Imaging: Physical Principles and Sequence Design, 2nd Edition*. Wiley-Blackwell, June 2014.

[9] A. D. Elster. Mri questions. `https://mriquestions.com/complete-list-of-questions.html`. Accessed: 20-03-2024.

[10] R. Mahir and K. Fardin. Mri scan: Components functions. `https://snc2dmri.weebly.com/components--functions.html`, October 2013. Accessed: 13-03-2024.

[11] S. D. Serai. Components of a magnetic resonance imaging system and their relationship to safety and image quality. *Pediatric Radiology*, 2021.

[12] B. Dymerska, B. A. Poser, M. Barth, S. Trattnig, and S. D. Robinson. A method for the dynamic correction of B0-related distortions in single-echo EPI at 7T. *NeuroImage*, 168:321–331, March 2018. ISSN 1095-9572. doi: 10.1016/j.neuroimage.2016.07.009.

[13] C. Paschal and H. Morris. K-Space in the Clinic. *Journal of magnetic resonance imaging : JMRI*, 19:145–59, February 2004. doi: 10.1002/jmri.10451.

[14] G. Glover. Overview of Functional Magnetic Resonance Imaging. *Neurosurgery clinics of North America*, 22(2):133–139, April 2011. ISSN 1042-3680. doi: 10.1016/j.nec.2010.11.001.

[15] P. Lima Cardoso, B. Dymerska, B. Bachratá, F. Fischmeister, N. Mahr, E. Matt, S. Trattnig, R. Beisteiner, and S. Robinson. The clinical relevance of distortion correction in presurgical fMRI at 7 T. *NeuroImage*, 168:490–498, March 2018. ISSN 1053-8119. doi: 10.1016/j.neuroimage.2016.12.070.

[16] Clinical Tree : Lead medical answers. Radiology key. `https://radiologykey.com/`, May 2016. Accessed: 08-04-2024.

[17] M. Haskell, JF Nielsen, and D. Noll. Off-resonance artifact correction for MRI: A review. *NMR in biomedicine*, 36(5):e4867, May 2023. ISSN 1099-1492. doi: 10.1002/nbm.4867.

[18] A. Saifuddin, S. Siddiqui, I. Pressney, and M. Khoo. The incidence and diagnostic relevance of chemical shift artefact in the magnetic resonance imaging characterisation of superficial soft tissue masses. *The British Journal of Radiology*, 93(1108):20190828, March 2020. ISSN 0007-1285. doi: 10.1259/bjr.20190828.

[19] B. Vachha and Susie Y. Huang. MRI with ultrahigh field strength and high-performance gradients: challenges and opportunities for clinical neuroimaging at 7 T and beyond. *European Radiology Experimental*, 5:35, August 2021. ISSN 2509-9280. doi: 10.1186/s41747-021-00216-2.

[20] M. Flasche and D. Fischer. *White Paper: Magnet homogeneity and shimming.* Siemens Healthcare GmbH, 2017.

[21] K. Wachowicz. Evaluation of active and passive shimming in magnetic resonance imaging. *Research and Reports in Nuclear Medicine*, 4:1–12, October 2014. doi: 10.2147/RRNM.S46526. Publisher: Dove Press.

[22] London Functional Imaging Laboratory, UCL Queen Square Institute of Neurology. Spm12. URL `https://github.com/spm/`.

[23] J. Andersson, C. Hutton, J. Ashburner, R. Turner, and K. Friston. Modeling Geometric Deformations in EPI Time Series. *NeuroImage*, 13:903–19, June 2001. doi: 10.1006/nimg.2001.0746.

[24] Barbara Dymerska, Korbinian Eckstein, Beata Bachrata, Bernard Siow, Siegfried Trattnig, Karin Shmueli, and Simon Daniel Robinson. Phase unwrapping with a rapid opensource minimum spanning tree algorithm (ROMEO). *Magnetic Resonance in Medicine*, 85(4):2294–2308, April 2021. ISSN 1522-2594. doi: 10.1002/mrm.28563. URL `https://github.com/korbinian90/ROMEO`.

[25] D. Garcia. Smoothn. URL `https://uk.mathworks.com/matlabcentral/fileexchange/25634-smoothn`.

[26] J. Ashburner, G. Barnes, C. Chen, J. Daunizeau, G. Flandin, K. Friston, D. Gitelman, V. Glauche, R. Henson, C. Hutton, A. Jafarian, S. Kiebel, J. Kilner, V. Litvak, J. Mattout, R. Moran, W. Penny, C. Phillips, A. Razi, and P. Zeidman. Spm12 manual. 2021.

[27] S. D. Robinson, B. Bachrata, K. Eckstein, S. Bollmann, S. Bollmann, B. Dymerska, S. Hodono, M. Cloos, M. Tourell, J. Jin, K. O'Brien, D. C. Reutens, S. Trattnig, C. Enzinger, and M. Barth. Improved dynamic distortion correction for fMRI using single-echo EPI and a readout-reversed first image (REFILL). *Human Brain Mapping*, 44(15):5095–5112, 2023. ISSN 1097-0193. doi: 10.1002/hbm.26440.

[28] Simin Liu, Yuhui Xiong, Erpeng Dai, Jieying Zhang, and Hua Guo. Improving distortion correction for isotropic high-resolution 3D diffusion MRI by optimizing Jacobian modulation. *Magnetic Resonance in Medicine*, 86(5), 2021. ISSN 1522-2594. doi: 10.1002/mrm.28884.